CHAPTER SIX

Multiscale remodeling of biomembranes and vesicles

Reinhard Lipowsky[*]
Max Planck Institute of Colloids and Interfaces, Science Park Golm, Potsdam, Germany
*Corresponding author. e-mail address: Reinhard.Lipowsky@mpikg.mpg.de

Contents

Abstract

Biomembranes and vesicles cover a wide range of length scales. Indeed, small nanovesicles have a diameter of a few tens of nanometers whereas giant vesicles can

Methods in Enzymology, Volume 701
ISSN 0076-6879, https://doi.org/10.1016/bs.mie.2024.04.006

have diameters up to hundreds of micrometers. The remodeling of giant vesicles on the micron scale can be observed by light microscopy and understood by the theory of curvature elasticity, which represents a top-down approach. The theory predicts the formation of multispherical shapes as recently observed experimentally. On the nanometer scale, much insight has been obtained via coarse-grained molecular dynamics simulations of nanovesicles, which provides a bottom-up approach based on the lipid numbers assembled in the two bilayer leaflets and the resulting leaflet tensions. The remodeling processes discussed here include the shape transformations of vesicles, their morphological responses to the adhesion of condensate droplets, the instabilities of lipid bilayers and nanovesicles, as well as the topological transformations of vesicles by membrane fission and fusion. The latter processes determine the complex topology of the endoplasmic reticulum.

1. Introduction

Eukaryotic organisms such as animals and plants contain a large amount of biomembranes that enclose their cells and many intracellular organelles. These membranes are fluid and create a flexible architecture, which is continuously remodeled by two different kinds of processes. First, the membranes adapt their shape to different interactions with their surroundings. Second, the membrane compartments change their topology via membrane fusion and membrane fission. The fission and fusion processes lead to heavy trafficking of vesicles between different organelles. This trafficking involves both the production of new vesicles via budding and fission from a donor membrane as well as the uptake of these vesicles by acceptor membranes via adhesion and fusion. In the cell, both fission and fusion involve a complex assortment of membrane-bound proteins that are believed to steer the different steps of these processes (Alberts et al., 1998; Bonifacino & Glick, 2004). The different proteins act in a concerted manner which makes it quite difficult to understand their individual roles even during a single fission or fusion event.

The remodeling of biological membranes and organelles can be mimicked via synthetic membrane systems which are built up from a relatively small number of molecular components and can be studied in a systematic and quantitative manner. In biochemistry and cell biology, these systems are conventionally called ‘in-vitro systems’ or ‘reconstituted systems’. Recently, a new motivation for the study of such model systems has been provided by the emerging bottom-up approach to synthetic biology because biomembranes represent an important module for this approach. Here, recent insights will be described for two synthetic membrane systems as provided by giant vesicles and small nanovesicles. For giant vesicles, the methodology is based on optical microscopy and curvature elasticity, for nanovesicles on molecular dynamics simulations and the novel concepts of leaflet tensions and stress asymmetry.

The remodeling of giant vesicles, which have a typical size of many micrometers, has been studied for a long time (Lipowsky & Sackmann, 1995; Bassereau & Sens, 2018; Dimova & Marques, 2019; Lipowsky & Dimova, 2021). Using optical microscopy, one can both image the different morphologies of giant vesicles and monitor their morphological transformations. The morphology of small nanovesicles, on the other hand, cannot be resolved by optical microscopy. Therefore, the main experimental methods to image small nanovesicles have been different variants of electron microscopy (Mui et al., 1995; Dragicevic-Curic et al., 2008; Baxa, 2018). The latter methods are, however, restricted to a single snapshot of each nanovesicle and, thus, cannot monitor how the shape of such a vesicle changes with time. In contrast, the spatio-temporal remodeling of nanovesicles can be elucidated by molecular dynamics simulations as recently demonstrated (Ghosh et al., 2019, 2023; Sreekumari & Lipowsky, 2022; Lipowsky et al., 2023).

The paper is organized as follows. The next Section 2 is devoted to the shapes of giant vesicles, emphasizing multispherical shapes, which consist of spherical membrane segments connected by closed membrane necks. The section also highlights the controlled remodeling of vesicle shape by the fine-tuning of spontaneous curvature, as recently achieved by exposing the vesicle membrane to His-tagged proteins. Section 3 describes the shape transformations of nanovesicles. These shape transformations are determined by the leaflet tensions acting within the two leaflets of the lipid bilayers and by the resulting stress asymmetry between the two leaflets. In the subsequent Section 4, large stress asymmetries are considered, which lead to stress-induced flip-flops of lipids from one leaflet to the other and to structural instabilities of the lipid bilayers. Section 5 deals with the remodeling of vesicle topology by fusion and fission processes. This section describes the curvature-induced division of giant vesicles, the stress-induced division of nanovesicles, the endocytosis of condensate droplets by nanovesicles, and the multiscale membrane architecture of the endoplasmic reticulum (ER). At the end, the results reviewed here are briefly summarized with an outlook on interesting topics for future research.

2. Shape remodeling of giant vesicles

Here and below, the term ‘giant vesicle’ always implies a ‘giant unilamellar vesicle’, for which we also use the abbreviation ‘GUV’.

2.1 Polymorphism of giant vesicles

Giant vesicles form many different shapes and undergo shape transformation in response to changes in the osmotic conditions, which control the vesicle volume, and to temperature changes, which affect the area of the vesicle membrane. This polymorphism has been studied for many years. Here, we will focus on two recent developments related to multispherical shapes of vesicles and to the controlled remodeling of vesicle shapes by the binding of His-tagged proteins to anchor lipids.

2.1.1 Two-sphere shapes with out-buds

The simplest multispheres are provided by two-sphere shapes, which consist of a spherical mother vesicle and a spherical out- or in-bud. The formation of an out-budded two-sphere shape is displayed in Fig. 1. In this example, we start from a GUV with a pear-like shape and reduce the vesicle volume by osmotic deflation. In response to this change in the osmotic conditions, the pear develops a membrane neck which closes in less than 16 s. As explained in the next subsection, such a two-sphere shape is only possible if the spontaneous curvature is positive and exceeds a certain positive threshold value.

2.1.2 Two-sphere shapes with in-buds

The formation of an in-budded two-sphere vesicle is shown in Fig. 2. In this example, we start from a GUV with a discocyte shape and increase the area of the vesicle membrane by an increase in temperature. In response to this area increase, the vesicle transforms into a stomatocyte shape and

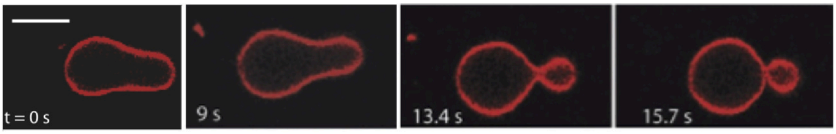

Fig. 1 Out-budding of a giant vesicle (red) with a pear-like shape, which transforms into a two-sphere shape, consisting of a spherical mother vesicle and a spherical out-bud, which are connected by a closed membrane neck. This shape transformation is obtained for a sufficiently large and positive spontaneous curvature that exceeds a certain positive threshold value (Bhatia et al., 2020).

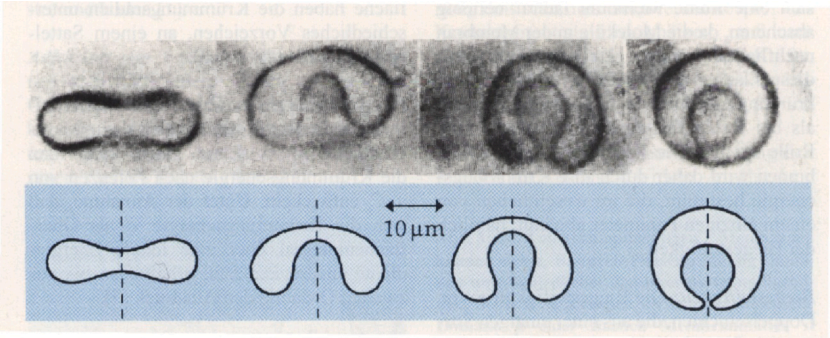

Fig. 2 In-budding of a giant vesicle with a discocyte shape, which transforms into a two-sphere shape, consisting of a spherical mother vesicle and a spherical in-bud connected by a closed membrane neck. This shape transformation is obtained for a sufficiently large and negative spontaneous curvature, which does not exceed a certain negative threshold value. *Reprinted with permission from Ref Berndl, K., Käs, J., Lipowsky, R., Sackmann, E., & Seifert, U. (1990). Shape transformations of giant vesicles: Extreme sensitivity to bilayer asymmetry. Europhysics Letters, 13, 659–664. [Copyright 1990, EDPSciences].*

subsequently into a two-sphere vesicle with an in-bud. As explained in the next subsection, the two-sphere shape in Fig. 2 is obtained for a sufficiently large and negative spontaneous curvature that does not exceed a certain negative threshold value.

2.2 Curvature elasticity

2.2.1 Spontaneous curvature model

The two-sphere shapes displayed in Figs. 1 and 2 were first obtained theoretically from the spontaneous curvature model (Seifert et al., 1991). This model was introduced by Helfrich (1973) and later supplemented by the experimentally important constraints for vesicle volume and membrane area (Deuling & Helfrich, 1976). The spontaneous curvature model is based on the curvature energy

$$E_{\rm cu} = \int dA \, [\, 2\,\kappa\,(M - m)^2 + \kappa_G\, G] \tag{1}$$

which represents an integral over the membrane area A, depends on two geometric quantities, the (local) mean curvature M and the (local) Gaussian curvature G of the membrane, and on three curvature-elastic parameters as provided by the bending rigidity κ, the spontaneous curvature m, and the Gaussian curvature modulus κ_G.

In the present section on vesicle shape, we will focus on shape transformations and exclude topological transformations, which implies that the area integral over the Gaussian curvature does not depend on the vesicle shape. As a consequence, the Gaussian curvature energy becomes

$$E_G = \int \mathrm{d}A \, \kappa_G \, G = 2\pi\chi\kappa_G = 2\pi\,(2 - 2\mathfrak{g})\,\kappa_G \tag{2}$$

with the Euler characteristic χ and the topological genus $\mathfrak{g}$ as follows from the Gauss-Bonnet theorem (do Carmo, 1976). Therefore, for shape transformations, which conserve the vesicle topology, the shapes of GUVs depend only on the bending energy

$$E_{\mathrm{be}} = \int \mathrm{d}A \; 2\,\kappa\,(M - m)^2. \tag{3}$$

This energy fulfills the inequality $E_{\mathrm{be}} \geq 0$, with $E_{\mathrm{be}} = 0$ for constant mean curvature $M = m$. In practise, the vesicle membrane cannot attain such a state with $M = m$ unless the vesicle forms a sphere or multisphere with constant mean curvature $M = M_{\mathrm{sp}} = m$.

2.2.2 Shape functional for giant vesicles

The experimentally observed vesicle shapes can be obtained by minimizing the bending energy E_{be} in Eq. (3), provided one takes additional constraints on the membrane area A and the vesicle volume V into account. At constant temperature, the membrane area of lipid bilayers is constant, reflecting the ultralow solubility of the lipid molecules. Likewise, the volume of the vesicle is conserved for constant pressure difference

$$\Delta P \equiv P_{\mathrm{ex}} - P_{\mathrm{in}} \tag{4}$$

between the pressures P_{in} and P_{ex} of the interior and exterior solutions, corresponding to constant osmotic conditions. We are then led to minimize the vesicle's shape functional (Deuling & Helfrich, 1976; Seifert et al., 1991).

$$F_{\mathrm{ve}} = \Delta P V + \Sigma A + E_{\mathrm{be}} = \Delta P V + \Sigma A + 2\,\kappa \int \mathrm{d}A \; (M - m)^2 \tag{5}$$

and to treat the parameters ΔP and Σ as Lagrange multipliers that allow us to perform the constrained minimization of the bending energy for a certain vesicle volume V and a certain membrane area A. Several recent studies have demonstrated that the shapes of GUVs calculated in this manner agree quantitatively with the experimentally observed shapes

(Bhatia et al., 2020; Steinkühler et al., 2020). In these latter experiments, the lipid membranes contained cholesterol which undergoes frequent flip-flops and implies that area-difference elasticity (Seifert et al., 1992; Dobereiner et al., 1997; Svetina & Zeks, 2002) plays no role.

2.2.3 Shape parameters and morphology diagrams

The shape functional F_{ve} as given by Eq. (5) depends on four (dimensionful) parameters: two material parameters, namely bending rigidity κ and spontaneous curvature m, as well as two geometric parameters, vesicle volume V and membrane area A. Furthermore, we can choose a basic energy and length scale. A natural choice for the energy scale is the bending rigidity κ. Furthermore, a convenient choice for the basic length scale is provided by the vesicle size

$$R_{\mathrm{ve}} \equiv \sqrt{A/(4\pi)}\,, \tag{6}$$

in terms of the membrane area A. Choosing these energy and length scales, the dimensionless bending energy E_{be}/κ depends only on two dimensionless shape parameters: (i) the volume-to-area ratio (or "reduced volume")

$$v \equiv \frac{V}{\frac{4\pi}{3}R_{\mathrm{ve}}^3} = 6\sqrt{\pi}\,V/A^{3/2} \tag{7}$$

of the vesicle; and (ii) the rescaled and dimensionless spontaneous curvature

$$\bar{m} \equiv mR_{\mathrm{ve}} = m\sqrt{A/(4\pi)}\,. \tag{8}$$

The two variables v and $\bar{m}$ define the two-dimensional morphology diagram for the vesicle shapes.

The volume-to-area ratio v can be varied experimentally in two different ways. First, it can be controlled by the osmotic conditions, that is, by osmotic deflation or inflation, which leads to a reduction or to an increase of the vesicle volume V for fixed membrane area A (Bhatia et al., 2020; Steinkühler et al., 2020). Alternatively, one might change the volume-to-area ratio v by varying the area per lipid and thus the membrane area A, which can be achieved, for example, by changes in temperature (Berndl et al., 1990) or by light-induced conformational transitions of photo-sensitive molecules in the lipid bilayers (Georgiev et al., 2018).

On the other hand, the spontaneous curvature $\bar{m}$ can be experimentally controlled, for fixed v, by adsorption and desorption processes, which modify the transbilayer asymmetry between the two leaflets of the bilayer membranes. One method by which the spontaneous curvature can be quantitatively controlled in an unprecedented manner is via the binding of green fluorescent protein (GFP) molecules from the exterior aqueous solution (Steinkühler et al., 2020) as described in Section 2.3 below.

2.2.4 Effective mean curvature of closed membrane necks

The two-sphere vesicles in Figs. 1 and 2 consist of one large sphere with radius R_l and one small sphere with radius R_s. Here and below, all radii are taken to be positive. For the out-budded two-sphere in the last panel of Fig. 1, both spherical segments have positive mean curvatures, as given by $M_l = 1/R_l$ and $M_s = 1/R_s$. For the in-budded two-sphere in the last panel of Fig. 2, the large sphere has positive mean curvature $M_l = 1/R_l$ as well but the small, inverted sphere has negative mean curvature $M_s = -1/R_s$.

Now, consider a closed membrane neck between two spherical segments with mean curvatures M_i and M_j. Using these two mean curvatures adjacent to the neck, we define the effective mean curvature of the closed neck by (Lipowsky, 2019).

$$M_{ij}^{\mathrm{eff}} \equiv \frac{1}{2}(M_i + M_j). \tag{9}$$

Note that the neck curvature M_{ij}^{eff} represents a purely geometric quantity. In fact, when the sphere diameters can be resolved by optical microscopy as in Figs. 1 and 2, the neck curvature M_{ij}^{eff} can be directly deduced from the optical images, see the examples in Fig. 3.

2.2.5 Positive and negative membrane necks

For the out-budded two-sphere vesicle in Fig. 1, the closed neck has a positive effective curvature

$$M_{ls}^{\mathrm{eff}} = \frac{1}{2}(M_l + M_s) = \frac{1}{2}\left(\frac{1}{R_l} + \frac{1}{R_s}\right) > 0 \quad (\mathrm{out} - \mathrm{bud}) \tag{10}$$

as follows from Eq. (9) with $M_i = M_l$ and $M_j = M_s$. For the in-budded two-sphere vesicle in Fig. 2, on the other hand, the effective neck mean curvature is negative and given by

$$M_{ls}^{\mathrm{eff}} = \frac{1}{2}(M_l + M_s) = \frac{1}{2}\left(\frac{1}{R_l} - \frac{1}{R_s}\right) < 0 \quad (\mathrm{in} - \mathrm{bud}) \tag{11}$$

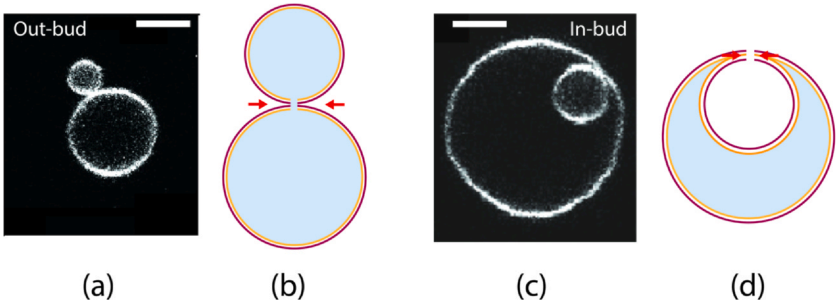

Fig. 3 Two-sphere shapes of giant vesicles with out- and in-buds: (a,b) Out-budded two-sphere shapes with positive membrane necks as observed by light microscopy in (a) and schematically depicted in (b). The scale bar in (a) is 5 μm, which implies the small-sphere radius $R_s = 1.6\,\mu\text{m}$ and the large-sphere radius $R_l = 4\,\mu\text{m}$ as well as the effective neck curvature $M_{ls}^{\text{eff}} = +0.44/\mu\text{m}$ as follows from Eq. (9); and (c,d) In-budded two-sphere shapes with negative membrane necks. The scale bar in (c) is again 5 μm which leads to the small-sphere radius $R_s = 2.5\,\mu\text{m}$ and the large scale radius $R_l = 7.9\,\mu\text{m}$ as well as to $M_{ls}^{\text{eff}} = -0.14/\mu\text{m}$. The red arrows in (b) and (d) indicate the constriction forces acting against the closed membrane necks.

The sign of the effective neck mean curvature is now used to distinguish positive from negative necks. By definition, a "positive neck" has a positive effective curvature $M_{ls}^{\text{eff}} > 0$ whereas a "negative neck" has a negative effective curvature $M_{ls}^{\text{eff}} < 0$. Therefore, the closed neck of an out-budded two-sphere shape as in Fig. 3a is positive whereas the closed neck of an in-budded two-sphere shape as in Fig. 3c is negative.

2.2.6 Local properties of closed membrane necks

The stability of closed membrane necks depends on the spontaneous curvature m. Each positive and negative neck is stably closed for (Lipowsky, 2014, 2019, 2022, 2022a)

$$m > M_{ij}^{\text{eff}} > 0 \quad \text{(stability of positive neck)} \tag{12}$$

and

$$m < M_{ij}^{\text{eff}} < 0 \quad \text{(stability of negative neck).} \tag{13}$$

These stability conditions for closed necks are intimately related to the bending energy for the closure of open necks. This bending energy can then be used to deduce the constriction force f acting against a positive and negative neck, which leads to (Lipowsky, 2019; Steinkühler et al., 2020; Lipowsky, 2022):

$$f = f_{\mathrm{pos}} \equiv 8\pi\kappa\,(m - M_{ij}^{\mathrm{eff}}) \geq 0 \quad \text{for positive necks} \tag{14}$$

and

$$f = f_{\mathrm{neg}} \equiv 8\pi\kappa\,(M_{ij}^{\mathrm{eff}} - m) \geq 0 \quad \text{for negative necks.} \tag{15}$$

The constriction forces f_{pos} and f_{neg} are indicated by the red arrows in Fig. 3b and Fig. 3d, respectively.

2.3 Controlled shape remodeling of giant vesicles

Both the stability conditions for closed necks and the constriction forces at these necks depend on the spontaneous curvature m. Thus, to investigate vesicle shapes with closed necks experimentally, one needs a method to control the spontaneous curvature in a quantitative manner. Such a method, which is based on the binding of His-tagged proteins to NTA-anchor lipids, has been recently developed (Steinkühler et al., 2020).

2.3.1 Low density of membrane bound GFP

The experiments were performed with exterior solutions of His-tagged GFP as well as with 1 mol% or 0.1 mol% anchor lipids in the lipid bilayers. For 1 mol%, the nanomolar GFP concentration X was varied within the range $0 < X \leq 23.4$ nM. For 0.1 mol% anchor lipids, the GFP concentration was varied up to $X = 39$ nM. In all cases, the membrane-bound GFP molecules had an average separation that was much larger than their lateral size of about 3 nm (Arpino et al., 2012), which implies that the vesicle membranes in Steinkühler et al. (2020) explored the dilute regime of membrane-bound proteins as indicated in Fig. 4.

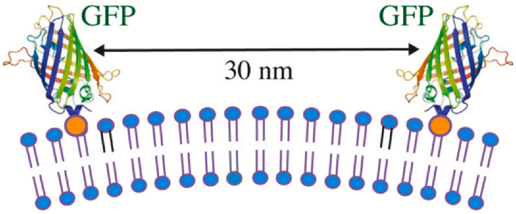

Fig. 4 Green fluorescent protein (GFP) molecules bound to the outer leaflet of a lipid bilayer. Each GFP has a His-tag which binds to an NTA-anchor lipid (orange headgroup). The average separation of the membrane-bound GFPs studied in Steinkühler et al. (2020) was at least 25 nm, which is much larger than the GFP's lateral size of about 3 nm.

The membrane-bound GFP molecules generate a surprisingly large spontaneous curvature m that was measured to be (Steinkühler et al., 2020)

$$m = \frac{\alpha}{\mu\text{m}} \frac{X}{\text{nM}} = \Gamma \times 27\ \text{nm} \tag{16}$$

where Γ is the GFP coverage of the outer membrane leaflet in units of membrane-bound molecules per area. The prefactor α is equal to $\alpha = 0.186$ for 0.1 mol% and $\alpha = 1.86$ for 1 mol% anchor lipids.

2.3.2 Shape parameters and morphology diagram

The morphology diagram of GUVs with membrane-bound GFP can now be determined experimentally (i) by changing the volume-to-area ratio v via the osmotic conditions and (ii) by controlling the spontaneous curvature $\bar{m} = mR_{\text{ve}}$ via the concentration X of His-tagged GFP in the exterior aqueous solution. The morphology diagram obtained in this manner is displayed in Fig. 5a for positive spontaneous curvature. The diagram contains the stability regime for the two-sphere vesicles with a positive

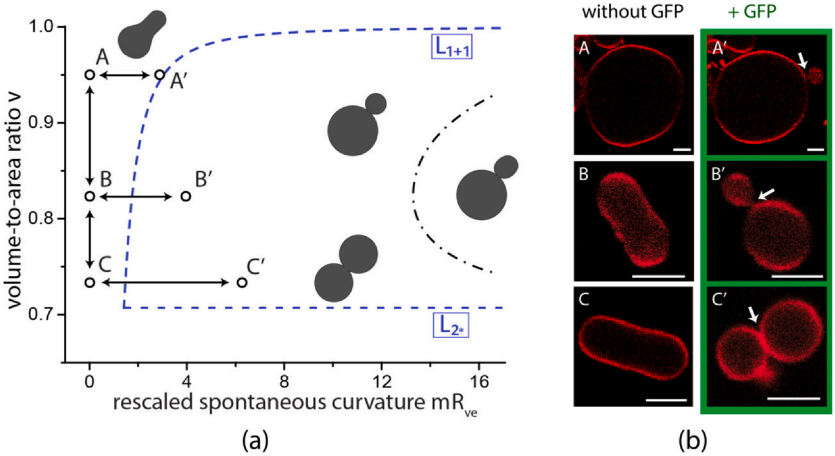

Fig. 5 (a) Morphology diagram of giant vesicles as a function of rescaled spontaneous curvature $\bar{m} = mR_{\text{ve}}$ and volume-to-area ratio v. Two-sphere vesicles with positive membrane necks are stable between the two dashed lines of limit shapes L_{1+1} and L_{2*} (blue). The latter subregion contains the dash-dotted line, at which the spherical out-bud becomes unstable and transforms into a prolate out-bud. The shapes denoted by A, B, and C correspond to three GUVs in the absence of GFP. Adding GFP to the exterior solution, the three GUVs transform into the dumbbell shapes A′, B′, and C′; and (b) Confocal images of the six vesicle shapes A, B, and C (left column) as well as A′, B′, and C′ (right column). The white arrows indicate the closed membrane necks (Steinkühler et al., 2020).

neck. This stability regime is bounded by two lines of limit shapes, denoted by L_{1+1} and L_{2^*}. The limit shapes L_{1+1} consist of one large and one small sphere, with two different mean curvatures $M_l = 1/R_l$ and $M_s = 1/R_s > M_l$, which represent two distinct roots of the quadratic shape equation for the mean curvature of a spherical membrane segment. The limit shapes L_{2^*} are formed by two equally sized spheres with identical mean curvatures $M_l = M_s = M^*$, which correspond to degenerate double roots of the quadratic shape equation (Lipowsky, 2022, 2022a).

When we leave the stability regime across the line L_{1+1} or across the line L_{2^*}, the closed membrane neck opens up. Within the stability regime, the two-sphere shapes represent persistent shapes that depend only on v and are independent of $\bar{m}$. However, the bending energy E_{be} of a given two-sphere shape increases with increasing spontaneous curvature $\bar{m}$, which eventually leads to the fission of the membrane neck as described further below in Section 5.4.

2.3.3 Control experiments with other fluorophores

The morphology diagram displayed in Fig. 5 has been obtained for His-tagged GFP bound to NTA anchor lipids. Qualitatively similar results have been observed for other His-tagged proteins such as His-tagged iLid bound to the same anchor lipids (Steinkühler et al., 2020). iLid belongs to a particularly interesting class of proteins, which are able to form photo-switchable protein dimers (Bartelt et al., 2018). Another, much smaller fluorophore provided by His-tagged FITC has also been studied (Pramanik et al., 2022). The experiments on His-tagged FITC turned out to be more difficult than expected because the fluorescence of FITC is strongly quenched by the anchor lipids which bind the fluorophores via Ni^{2+} ions. Furthermore, the fluorescence of FITC is also observed to be strongly pH-dependent (Pramanik et al., 2022).

2.4 Two-sphere shapes and condensate droplets

As described in the previous subsections, two-sphere shapes of giant vesicles can be formed when the two leaflets of the vesicle membranes are exposed to different aqueous solutions. One example for this solution asymmetry is provided by interior sucrose solutions and exterior glucose solutions as in Fig. 1. Another example for such a solution asymmetry is provided by exterior solutions of His-tagged GFP, which binds to the outer leaflet of the membranes, as in Fig. 5. Two-sphere shapes of giant vesicles have also been observed (Li et al., 2012b; Dimova & Lipowsky, 2017) when the vesicle membranes are exposed to aqueous solutions of macromolecules, which undergo liquid-liquid phase separateion into aqueous two-phase systems and lead to the formation of condensate droplets (Lipowsky, 2023).

2.4.1 Condensate droplets from aqueous phase separation

The term 'condensate droplet' is used to emphasize that the droplet is enclosed by a liquid–liquid rather than by a liquid–gas interface. Aqueous two-phase (or biphasic) systems based on biopolymers such as PEG and dextran have been applied for several decades in biochemical analysis and biotechnology (Albertsson, 1986) and are intimately related to water-in-water emulsions (Esquena, 2016). The aqueous phase separation leads to the formation of two coexisting liquid phases, denoted here by α and β.

The aqueous phase separation of PEG-dextran solutions provides an example for *segregative* phase separation, in which one phase is enriched in one macromolecular component such as PEG whereas the other phase is enriched in the other macromolecular component such as dextran. The segregative behavior implies that the different species of macromolecules effectively repel each other. Another type of aqueous two-phase system is created by *associative* phase separation, for which one phase is enriched in the macromolecular components whereas the other phase represents a dilute solution of the macromolecules (Crowe & Keating, 2018; Bungenberg de Jong & Kruyt, 1929; Sing, 2017; Li et al., 2018). The associative behavior implies that the different macromolecular species effectively attract each other. Associative phase separation is observed, for instance, in solutions of two, oppositely charged polyelectrolytes (Sing, 2017; Li et al., 2018),

Condensate droplets have also been observed in living cells where they provide separate liquid compartments which are not bounded by membranes. Examples for these condensates include germ P-bodies (Brangwynne et al., 2009; Fritsch et al., 2021), nucleoli (Berry et al., 2015), and stress granules (Jain et al., 2016). These biomolecular condensates are believed to form via liquid–liquid phase separation in the cytoplasm (Brangwynne et al., 2009; Banani et al., 2017) and can be reconstituted in vitro (Li et al., 2012a; Patel et al., 2015; Lin et al., 2015; Molliex et al., 2015). They are enriched in certain types of proteins that have intrinsically disordered domains and interact via multivalent macromolecular interactions (Han et al., 2012; Lin et al., 2015; Molliex et al., 2015; Guo & Shorter, 2015; Banani et al., 2017).

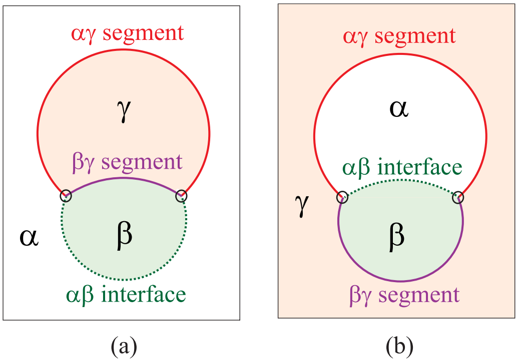

Fig. 6 Geometry of vesicle-droplet systems, which involve three liquid phases α (white), β (green), and γ (light red). The phases α and β represent two coexisting phases that arise via segregative or associative liquid–liquid phase separation; the γ phase is an inert spectator phase: (a) Phase separation of the exterior solution and adhesion of an exterior β droplet to the outer leaflet of the vesicle membrane; and (b) Phase separation of the interior solution creating one interior α and one interior β droplet, both of which are in contact with the inner leaflet of the membrane. For partial wetting as shown here, the $\alpha\beta$ interface (dashed green line) and the vesicle membrane form a contact line (open circles), which partitions the vesicle membrane into the $\alpha\gamma$ and $\beta\gamma$ segments. (Lipowsky, 2023).

2.4.2 *Geometry of vesicle-droplet systems*

When a condensate droplet comes into contact with a vesicle membrane, attractive interactions between droplet and membrane lead to the adhesion of the droplet to the membrane. The geometry of these vesicle-droplet systems involves three liquid phases α, β, and γ as shown in Fig. 6. The two phases α and β are formed by segregative or associative liquid–liquid phase separation and are separated by the $\alpha\beta$ interface. When the droplet adheres to the membrane, the $\alpha\beta$ interface forms a contact line with the membrane, which divides the membrane up into two segments, the $\alpha\gamma$ segment exposed to the α and γ phases as well as the $\beta\gamma$ segment in contact with the β and γ phases. In Fig. 6a and 6b, the coexisting phases α and β are located outside and inside the vesicle, respectively. Therefore, Fig. 6a displays one exterior β droplet in contact with the outer leaflet of the bilayer membrane whereas Fig. 6b shows one interior α and one interior β droplet in contact with the inner leaflet of the membrane.

2.4.3 *Morphological responses of vesicle membranes*

The adhesion of the condensate droplet generates strong morphological responses of the vesicle membrane. One example for this response is

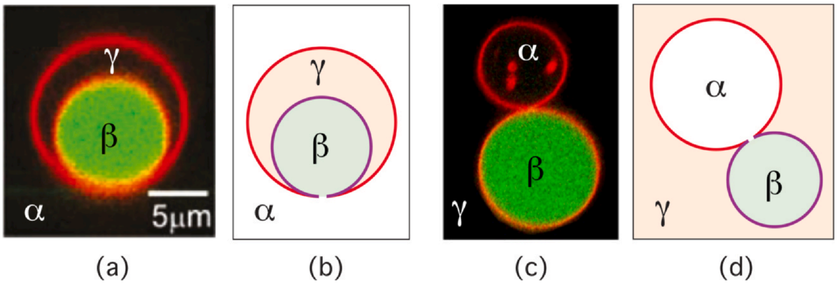

Fig. 7 Complete engulfment of condensate droplets (green) by GUV membranes (red): (a) Two-sphere shape of a vesicle membrane that engulfs the β droplet via an in-bud; (b) Schematic drawing for the optical image in (a), indicating the negative contact line neck between the two spheres; (c) Two-sphere shape of the membrane, which forms two spherical segments around both the β (green) and the α (black) droplet, connected by a positive contact line neck (Dimova & Lipowsky, 2017); and (d) Schematic drawing for the optical image in (c). For complete engulfment, the free energy of the vesicle-droplet system is strongly reduced by eliminating the $\alpha\beta$ interface and replacing it by a closed contact line neck. *Reprinted with permission from Ref. Li, Y., Kusumaatmaja, H., Lipowsky, R., & Dimova, R. (2012b). Wetting-induced budding of vesicles in contact with several aqueous phases. The Journal of Physical Chemistry B, 116, 1819–1823. [Copyright 2012, American Chemical Society].*

provided by the apparent kinks, which are observed in the optical microscope along the contact line between the adhering droplet and the vesicle membrane, as schematically shown in Fig. 6. On nanoscopic scales, these kinks represent membrane segments with a very high curvature, caused by the capillary forces that the $\alpha\beta$ interface exerts onto the contact line. (Kusumaatmaja et al., 2009; Lipowsky, 2018) Another, particularly interesting response is provided by the complete engulfment of the droplet by the membrane as displayed in Fig. 7. (Li et al., 2012b; Dimova & Lipowsky, 2017).

2.4.4 Complete engulfment of condensate droplets

The complete engulfment of an exterior β droplet as depicted in Fig. 7a leads to a spherical in-bud. The complete engulfment of the interior α and β droplets leads to spherical out-buds as in Fig. 7c. For both morphologies of the vesicle-droplet system, the closed membrane neck has been formed via the closure of the contact line. Therefore, these closed necks represents contact line necks. One consequence of this geometry is that the constriction force f acting against the contact line neck is enhanced by the line tension λ_{cl} of the contact line. More precisely, the presence of the contact

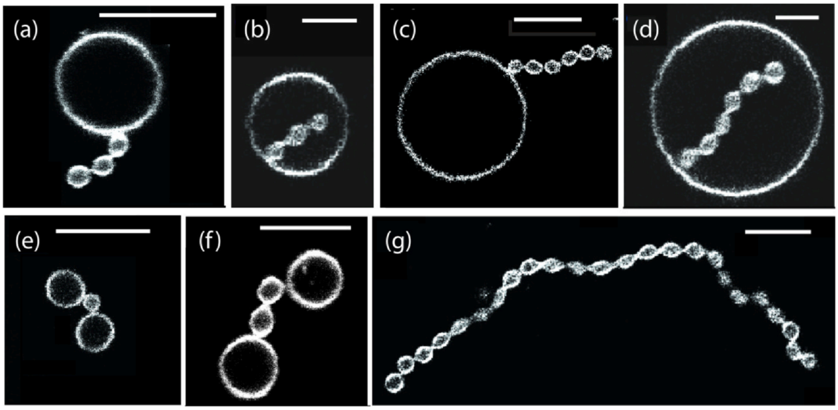

Fig. 8 Positive and negative multispheres of giant vesicles: (a) Positive (1 + 3)-sphere consisting of one large and one out-budded chain of three small spheres; (b) Negative (1 + 3)-sphere with one large and one in-budded chain of three small spheres; (c) Positive (1 + 6)-sphere with one large sphere and one out-budded chain of six small spheres; (d) Negative (1 + 6)-sphere with one large sphere and one in-budded chain of six small spheres; (e) Positive (2 + 1)-sphere consisting of two large and one small spheres; (f) Positive (2 + 2)-sphere with two large and two small spheres; and (g) Positive (24*)-sphere consisting of 24 equally sized spheres. All scale bars are 10 μm (Bhatia et al., 2020).

line within the membrane neck increases the constriction forces $f_{\rm pos}$ and $f_{\rm neg}$ in Eqs. (14) and (15) by $\Delta f_{\rm cl} = 2\pi\lambda_{\rm cl}$ for both positive and negative membrane necks.

2.5 Multispherical shapes of giant vesicles

The two-sphere shapes in Figs. 1–3, 5, and 7 represent the simplest examples for multispherical shapes. In general, GUVs can form a large variety of multispheres consisting of more than two spheres connected by more than one membrane neck (Lipowsky, 2014, 2018a; Bhatia et al., 2020; Lipowsky, 2022). Some optical microscopy images of such multispheres are displayed in Fig. 8.

It will be useful to distinguish *positive multispheres* as formed by vesicle membranes with positive spontaneous curvature from *negative multispheres* for membranes with negative spontaneous curvature. As will be shown below, each positive multisphere exhibits only positive membrane necks with neck curvature $M_{ij}^{\rm eff} > 0$ whereas each negative multisphere involves only negative necks with neck curvature $M_{ij}^{\rm eff} < 0$.

2.5.1 Positive multispheres for positive spontaneous curvature

For positive spontaneous curvatures, the giant vesicles can form $(N_l + N_s)$-multispheres consisting of N_l large spheres and N_s small spheres with $N_l \geq 1$ and $N_s \geq 1$. Examples for such multispheres are displayed in Fig. 8a,c,e-g. Inspection of these panels shows that, for each $(N_l + N_s)$-multisphere, all individual spheres have a positive mean curvature and all closed membrane necks are positive in the sense that they have a positive neck curvature $M_{ij}^{\text{eff}} > 0$. Such a positive neck is stably closed for sufficiently large and positive spontaneous curvatures m, which exceed the neck curvature M_{ij}^{eff} as in Eq. (12), and is then compressed by the constriction force $f = f_{\text{pos}}$ as given by Eq. (14).

For each positive multisphere in Fig. 8a,c,e, and f, all large spheres have the same mean curvature $M_l = 1/R_l$ and all small spheres have the same mean curvature $M_s = +1/R_s$. Each negative multisphere as in Fig. 8b and d consists of one large sphere with $M_l = 1/R_l$ and a variable number of inverted small spheres with $M_s = -1/R_s$. As long as $R_l > R_s$, the large and small spheres correspond to two distinct roots of the quadratic shape equation for the mean curvature of a spherical segment. When the shape equation has a degenerate double root, one obtains positive (N_*)-multispheres with N_* equally sized spheres as in Fig. 8g with $N_* = 24$.

2.5.2 Morphology diagrams for positive multispheres

Each $(N_l + N_s)$-multisphere represents a stable vesicle morphology for a certain stability regime within the morphology diagram. Some stability regimes for positive multispheres are displayed in Fig. 9. Each stability regime is bounded by two lines of limit shapes, which are denoted by L_{Nl+Ns} and L_{N_*} with $N_* = N_l + N_s$. Because the multispheres involve different types of membrane necks connecting different pairs of adjacent spheres, the limit shapes L_{Nl+Ns} are further specified by the superscript *ls* and *ss*. The superscript *ls* implies that the most unstable necks are provided by *ls*-necks. The superscript *ss* is used to indicate that the most unstable necks correspond to *ss*-necks.

2.5.3 Negative multispheres for negative spontaneous curvature

For vesicle membranes with negative spontaneous curvature, the membranes can form $(1 + N_s)$-multispheres consisting of one large sphere with positive mean curvature $M_l = 1/R_l$ and N_s small, inverted spheres with negative mean curvature $M_s = -1/R_s$. Examples for the latter type of multispheres are displayed in Fig. 8b and d. Inspection of this figure shows

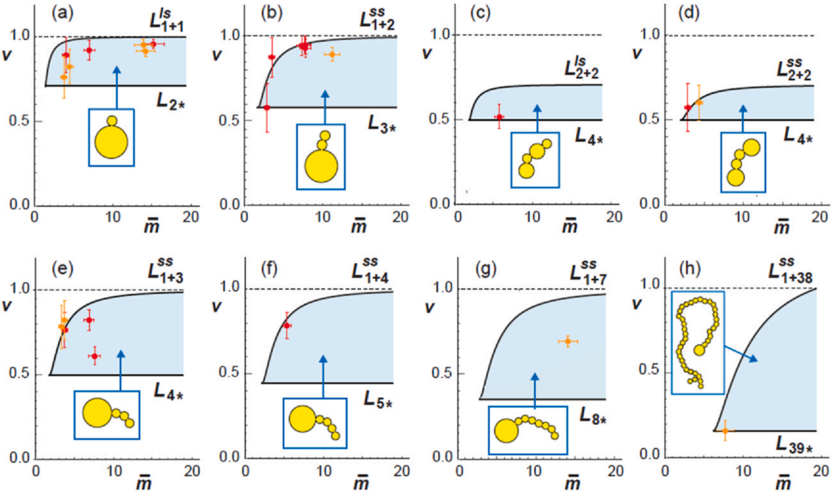

Fig. 9 Stability regimes (light blue) for positive multispheres, formed by vesicle membranes with positive spontaneous curvature. Each stability regime represents a subregion of the morphology diagram as defined by the rescaled spontaneous curvature $\bar{m} \geq 0$ and by the volume-to-area ratio v. Furthermore, each stability regime is bounded by two lines of limit shapes, L_{Nl+Ns} and L_{N*} with N_* equally sized spheres. The red and orange data points represent the values for v and $\bar{m}$ as obtained experimentally for two different sugar asymmetries across the bilayers. (Bhatia et al., 2020).

that all individual spheres of the $(1 + N_s)$-multisphere are connected by negative membrane necks in the sense that they have a negative neck curvature $M_{ij}^{\mathrm{eff}} < 0$. Such a negative neck is stably closed for sufficiently large and negative spontaneous curvatures m, which are more negative than M_{ij}^{eff} as in Eq. (13). The constriction force $f = f_{\mathrm{neg}}$ acting against this neck is given by Eq. (15).

3. Shape transformations of nanovesicles

Lipid bilayers and biomembranes form nanovesicles with a diameter between 20 and 200 nm. Electron microscopy studies have shown that these vesicles can attain both spherical and nonspherical shapes. However, the insight obtained from electron microscopy studies about the shapes of nanovesicles is quite limited because the corresponding images provide only a single snapshot of each vesicle. In contrast, molecular dynamics simulations can monitor the morphologies of individual nanovesicles as we vary a certain control parameter such as the vesicle volume. Recently, we

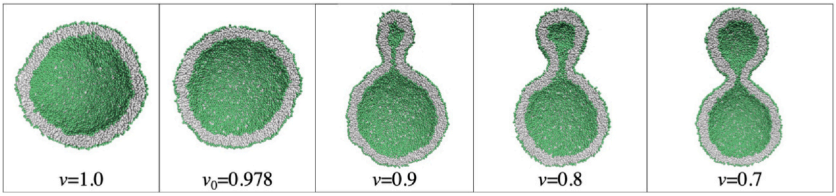

Fig. 10 Shape transformation of a spherical nanovesicle into a dumbbell shape with a closed membrane neck. The first panel with volume parameter $v = 1$ displays the initial spherical shape, assembled from $N_{ol} = 6300$ lipids in the outer leaflet and $N_{il} = 3800$ lipids in the inner leaflet, which leads to a compressed outer leaflet and a stretched inner leaflet, see Fig. 13 further below. Reducing the volume from $v = 1$ to $v_0 = 0.978$, the nanovesicle attains a state with vanishing bilayer tension. A further reduction of the vesicle volume to $v \leq 0.9$ leads to dumbbell shapes with closed membrane necks. The lipid headgroups are green, the hydrophobic chains are grey. (Ghosh et al., 2019).

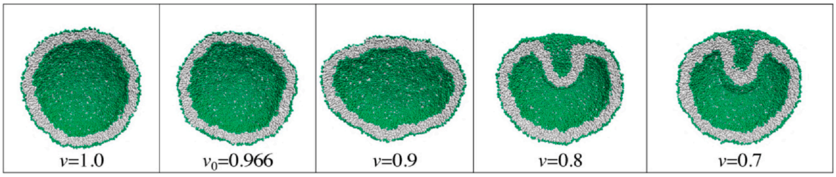

Fig. 11 Shape transformation of a spherical nanovesicle into a stomatocyte shape. The first panel with volume parameter $v = 1$ displays the initial spherical shape, assembled from $N_{ol} = 5700$ lipids in the outer leaflet and $N_{il} = 4400$ lipids in the inner leaflet, which leads to a stretched outer and a compressed inner leaflet, see Fig. 13 below. Compared to Fig. 10, 600 lipids have been reshuffled from the outer to the inner leaflet. A vesicle bilayer with vanishing bilayer tension is obtained for volume parameter $v_0 = 0.966$. A further reduction of the vesicle volume to $v \leq 0.8$ leads to stomatocyte shapes with membrane invaginations. Same color code as in Fig. 10. (Ghosh et al., 2019).

studied how nanovesicles respond to such volume changes mimicking the experimental procedure of osmotic deflation. As a result, we found that spherical nanovesicles can transform into a multitude of nonspherical shapes as illustrated by the simulaton snapshots in Figs. 10 and 11 (Ghosh et al., 2019). For the simulations, we used coarse-grained molecular dynamics as provided by dissipative particle dynamics (Shillcock & Lipowsky, 2002, 2005).

The shape transformations of the nanovesicle in Fig. 10 resemble the remodeling of the GUV in Fig. 1. Likewise, the nanovesicle shapes in Fig. 11 look similar to those of the GUV in Fig. 2. Thus, the vesicle volume turns out to be an important control parameter for both giant vesicles and nanovesicles but the spontaneous curvature of GUV membranes is replaced by the leaflet tensions and the stress asymmetry of nanovesicle membranes.

3.1 Volume parameter for nanovesicles

In the experimental studies of GUVs, the vesicle volume is typically changed by osmotic deflation and inflation. In the coarse-grained molecular dynamics simulations used to obtain the snapshots in Figs. 10 and 11, the vesicle volume was varied by changing the number N_{W} of water beads enclosed by the inner leaflet of the vesicle membrane. Each water bead with diameter $d \simeq 0.8\,\mathrm{nm}$ represents three water molecules which implies the vesicle volume $V \equiv N_{\mathrm{W}}\, d^3/3$. To monitor changes of the vesicle volume, the rescaled volume ν was used which is defined by

$$\nu \equiv \frac{N_{\mathrm{W}}}{N_{\mathrm{W}}^{\mathrm{isp}}} \tag{17}$$

where $N_{\mathrm{W}}^{\mathrm{isp}}$ is the number of water beads enclosed by the initial spherical vesicle. Thus, the initial vesicle is characterized by $\nu = 1$ and any volume reduction with $N_{\mathrm{W}} < N_{\mathrm{W}}^{\mathrm{isp}}$ leads to $\nu < 1$. Monitoring volume changes via the parameter ν is convenient because we can directly change the number N_{W} of water beads within the vesicle and thus compute the value of ν without the necessity to determine any membrane surface.

3.2 Leaflet tensions and stress asymmetry

The lipid numbers N_{ol} and N_{il} assembled in the outer and inner leaflet of the vesicle bilayer provide useful parameters, which can be directly controlled during the simulation setup. These lipid numbers determine the leaflet tensions Σ_{ol} and Σ_{il} within the two leaflets. The sum $\Sigma_{ol} + \Sigma_{il}$ of the two leaflet tensions is equal to the bilayer tension Σ.

3.2.1 Assembly of planar bilayers and nanovesicles

In water, lipids assemble into molecular bilayers as shown in Fig. 12. The headgroups of the bilayers form two interfaces with the surrounding aqueous solutions, thereby shielding the hydrophobic chains from these solutions. In Fig. 12a, we see a planar bilayer spanning the simulation box with periodic boundary conditions. If we considered a finite bilayer patch completely immersed in an aqueous solution, the hydrophobic core of the bilayer would come into contact with this solution, and the tension of this bilayer edge would make a large positive contribution to the system's free

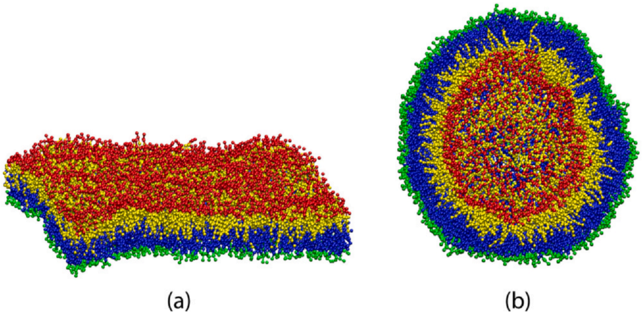

Fig. 12 Leaflets of lipid bilayers visualized by different colors: (a) Oblique view onto a planar lipid bilayer consisting of 841 lipid molecules in each leaflet; and (b) Half cut view of a nanovesicle with $N_{ol} = 1685$ lipids in its outer and $N_{il} = 840$ lipids in its inner leaflet, which sum up to the total lipid number $N_{ol} + N_{il} = 2525$. The molecular interface between the two leaflets is located between the yellow and blue lipid chains. In both panels a and b, the two leaflets are tensionless which implies that each lipid attains its optimal area and its optimal volume. The water beads around the lipid bilayers are taken to be transparent for visual clarity (Zamaletdinov et al., 2023).

energy. To avoid these bilayer edges, the planar bilayer patch will close up to form a nanovesicle as in Fig. 12b.

In Fig. 12a and b, the molecular interface between the two leaflets of the lipid bilayer is clearly visible because the lipids in one leaflet are depicted with red headgroups and yellow chains whereas the lipids in the other leaflet have green headgroups and blue chains, even though all lipids have the same molecular architecture. Thus, the interface between the two leaflets separates the yellow from the blue chains.

The midsurface of a lipid bilayer as obtained from the molecular interface between the two leaflets must be distingulshed both from the bilayer's "neutral surface" and from the "surface of tension" for liquid–liquid interfaces. The "neutral surface" is defined by its elastic state of being neither stretched nor compressed during an elastic deformation of the bilayer membrane (Kozlov et al.. 1989; Winterhalter & Helfrich, 1992; Templer, 1995), as originally described for solid plates and shells (Landau & Lifshitz, 1986).

The "surface of tension" for liquid–liquid interfaces, on the other hand, corresponds to a Gibbs dividing surface, which is used to reconcile the mechanical and thermodynamic definitions of interfacial tension (Gibbs, The Scientific Papers, 1906; Buff, 1956; Boruvka & Neumann, 1977; Rowlinson & Widom, 1989). However, in contrast to interfacial tension, the thermodynamic route to membrane tension is rather problematic. Indeed, a sufficiently large membrane segment that is stretched by a positive mechanical tension can always lower its free energy by rupture and pore formation. Furthermore, a fluid and tensionless membrane starts to behave like a random surface without any average orientation as soon as its size exceeds the so-called persistence length (de Gennes & Taupin, 1982; Gompper & Kroll, 1995). Therefore, the thermodynamic definition of membrane tension, which involves the limit of large membrane segments, is beset with conceptual difficulties. In order to avoid these difficulties, our computational studies were based on the mechanical definition of the bilayer tension as provided by Eqs. (A3) and (A6) in Appendix A *without* a Gibbs dividing surface.

3.2.2 Positive and negative leaflet tensions

Each bilayer leaflet can experience a positive or negative leaflet tension, depending on the number of lipids that are assembled into the leaflet. A positive leaflet tension implies that the leaflet is stretched whereas a negative leaflet tension describes a compressed leaflet. In order to avoid membrane rupture, the osmotic conditions in the aqueous solutions surrounding the bilayer membrane must be adjusted in such a way that the bilayer is subject to a relatively low bilayer tension. However, even for a tensionless bilayer with vanishing bilayer tension $\Sigma = \Sigma_{ol} + \Sigma_{il} = 0$, the two leaflets of the bilayer may still experience significant leaflet tensions. Indeed, a tensionless bilayer with $\Sigma = 0$ only implies that $\Sigma_{il} = -\Sigma_{ol}$. The latter relation can be fulfilled whenever one leaflet is stretched and the other leaflet is compressed by the opposite leaflet tension.

On the other hand, if both leaflet tensions, Σ_{ol} and Σ_{ol}, vanish, the bilayer tension $\Sigma = \Sigma_{ol} + \Sigma_{il}$ must vanish as well. The special bilayer state with vanishing leaflet tensions, $\Sigma_{ol} = \Sigma_{il} = 0$ defines a unique reference state for all bilayers assembled with the same total number $N = N_{ol} + N_{il}$ of lipids in the two leaflets. In this reference state, the lipids are packed in an optimal manner.

3.2.3 Computation of leaflet tensions

The bilayer tension Σ can be obtained from the stress profile across the bilayer by integrating this profile along the coordinate perpendicular to the bilayer membrane as described in Appendix A. To actually compute the leaflet tensions Σ_{ol} and Σ_{il}, we need to identify the spatial regions that are, on average, occupied by the two leaflets and to decompose the overall bilayer tension into two separate contributions from the two leaflets. The average position of the leaflet-leaflet interface defines the midsurface for both planar bilayers and spherical nanovesicles. The position of the midsurface is easy to find for symmetric planar bilayers but requires some computational effort in all other cases, both for the midsurfaces of asymmetric planar bilayers and for the midsurfaces of vesicle bilayers.

During the last couple of years, several protocols have been developed to determine the midsurface of a lipid bilayer (Rozycki & Lipowsky, 2015; Sreekumari & Lipowsky, 2018; Ghosh et al., 2019; Miettinen & Lipowsky, 2019; Sreekumari & Lipowsky, 2022; Lipowsky et al., 2023; Zamaletdinov et al., 2023). The CHAIN protocol is based on the density profile of the chain beads (Rozycki & Lipowsky, 2015; Sreekumari & Lipowsky, 2018; Ghosh et al., 2019; Sreekumari & Lipowsky, 2022; Lipowsky et al., 2023). Two alternative protocols are the HEAD protocol (Ghosh et al., 2019), which starts from the two head group layers, and the COM protocol (Ghosh et al., 2019; Miettinen & Lipowsky 2019), which computes the center-of-mass of the lipid bilayer. All three protocols were systematically compared in Ref Ghosh et al. (2019) and shown to differ by at most 3% for the midsurface of a vesicle bilayer. Another useful protocol, which has been introduced quite recently, is the VORON protocol, which is based on the computation of volumes per lipid via Voronoi tessellation (Zamaletdinov et al., 2023). The CHAIN and VORON protocols are described in more detail in Appendix B.

3.2.4 Dependence of leaflet tensions on lipid numbers

The simulation snapshots in Figs. 10 and 11 display vesicles, which are assembled from the same total number of lipids, $N_{ol} + N_{il} = 10100$. The corresponding simulation data for the leaflet tensions Σ_{ol} and Σ_{il} are displayed in Fig. 13 as functions of the lipid number N_{ol} in the outer leaflet. The data in Fig. 13a are obtained for fixed volume parameter $\nu = 1$, corresponding to the initial spherical vesicles in Figs. 10 and 11. The data in Fig. 13b represent the leaflet tensions for volume parameter $\nu = \nu_0$, for which the bilayer tension vanishes. Therefore, the bilayer tension $\Sigma = \Sigma_{ol} + \Sigma_{il}$ is close to zero in Fig. 13b but has a finite value in Fig. 13a. All data represent simulation results obtained via the CHAIN protocol.

In both panels of Fig. 13, the lipid number N_{ol} is increased by reshuffling lipids from the inner to the outer leaflet for fixed total lipid number $N_{ol} + N_{il} = 10100$. This reshuffling increases the lipid density in the outer leaflet and decreases this density in the inner leaflet. As a

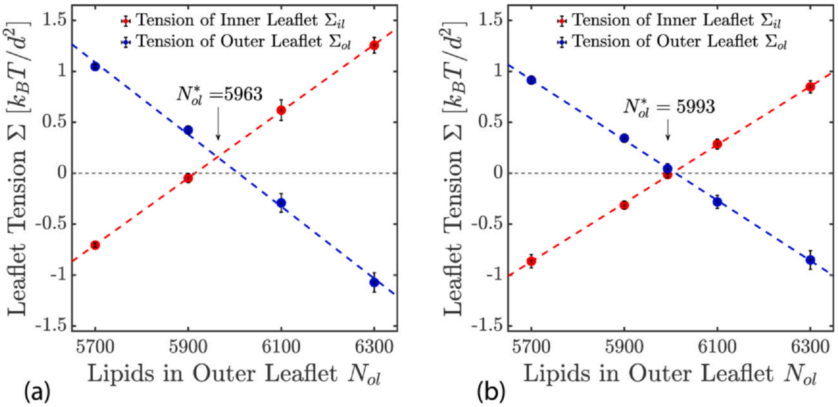

Fig. 13 Leaflet tensions Σ_{il} and Σ_{ol} of the inner and outer leaflets for vesicle bilayers with constant total lipid number $N_{il} + N_{ol} = 10100$. The lipid number N_{ol} is increased by reshuffling lipids from the inner to the outer leaflet: Spherical vesicles with volume parameter $v = 1$ in (a) and $v = v_0 < 1$ in (b). For $v = v_0$, the bilayer tension $\Sigma = \Sigma_{ol} + \Sigma_{il}$ is close to zero. The crossing points between the two leaflet tensions are estimated by linear interpolation, which leads to $N_{ol} = N^*_{ol} = 5963$ in (a) and to $N_{ol} = N^*_{ol} = 5993$ in (b). The reference state with tensionless leaflets is obtained close to the crossing point in (b). For all data, the midsurface of the bilayers was calculated using the CHAIN protocol (Ghosh et al., 2019).

consequence, the outer leaflet becomes more compressed, which leads to a reduction of the outer leaflet tension Σ_{ol}, and the inner leaflet becomes more stretched, which implies an increase in the inner leaflet tension Σ_{il}. In Fig. 13a, the two data sets for the leaflet tensions Σ_{ol} and Σ_{il} are well fitted by two straight lines that cross each other at $N_{\rm ol} = N^*_{\rm ol} = 5963$. At this crossing point, the two leaflet tensions are equal to each other with $\Sigma_{\rm il} = \Sigma_{\rm ol} \simeq 0.18\, k_{\rm B}T/d^2$. In Fig. 13b, the two data sets for Σ_{ol} and Σ_{il} cross each other at $N_{\rm ol} = N^*_{\rm ol} = 5993$, where both leaflet tensions are close to zero.

The data in Fig. 13 are obtained from several statistically independent simulations of five different spherical vesicles, corresponding to five different lipid numbers N_{ol} and $N_{il} = 10100 - N_{ol}$. In addition, the four data points in Fig. 13a are for vesicles with volume $\nu = 1$ whereas the five data points in Fig. 13b are for vesicles with volume $\nu = \nu_0 < 1$ and vanishing bilayer tension. For each of these nine vesicles, the area per lipid, a_{il}, in the inner leaflet was larger than the area per lipid, a_{ol}, in the outer leaflet (Ghosh et al., 2019; Sreekumari & Lipowsky, 2022; Zamaletdinov et al., 2023).

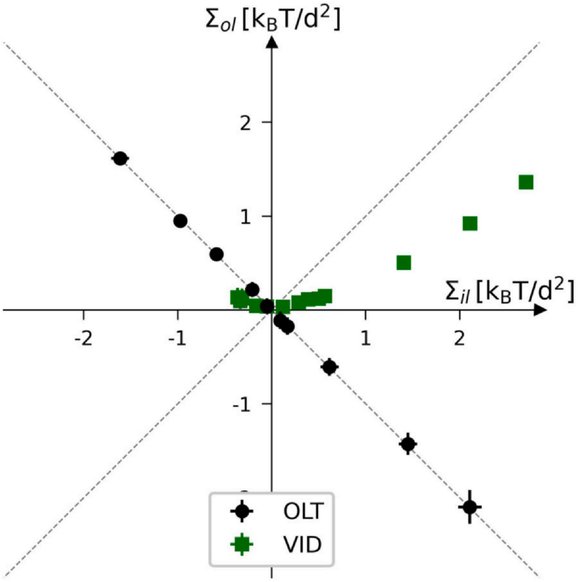

Fig. 14 Two-dimensional leaflet tension space defined by the inner and outer leaflet tensions Σ_{il} and Σ_{ol} for vesicle bilayers with constant total lipid number $N_{il} + N_{ol} = 2525$. Negative and positive leaflet tensions describe compressed and stretched leaflets. The reference state with tensionless leaflets, corresponding to $\Sigma_{il} = \Sigma_{ol} = 0$, is obtained for a vesicle bilayer with $N_{il} = 840$ lipids in the inner leaflet and $N_{ol} = 1685$ lipids in the outer one. The black data represent elastic OLT deformations obtained from the reference state by reshuffling lipids from one leaflet to the other and adjusting the vesicle volume to obtain tensionless bilayers with $\Sigma = \Sigma_{il} + \Sigma_{ol} = 0$. The green data represent the elastic deformations arising from changes in vesicle volume, corresponding to vesicle inflation or deflation (VID). All data obtained via the VORON protocol (Zamaletdinov et al., 2023).

3.2.5 Two-dimensional leaflet tension space

The two leaflet tensions Σ_{il} and Σ_{ol} define a two-dimensional parameter space for nanovesicles. This space is depicted in Fig. 14 for vesicle bilayers with a total number of $N_{ol} + N_{il} = 2525$ lipids. The origin $(\Sigma_{il}, \Sigma_{ol}) = (0, 0)$ of this leaflet tension space defines the relaxed reference state with tensionless leaflets. This reference state is obtained for a vesicle bilayer with $N_{il} = 840$ lipids in the inner and $N_{ol} = 1685$ lipids in the outer leaflet (Zamaletdinov et al., 2023).

To characterize the elastic response of the reference state, it will be useful to distinguish two types of elastic deformations, corresponding to the black and green data in Fig. 14. The black data in Fig. 14 describe elastic deformations of the reference state with

$$\Sigma_{il} = -\Sigma_{ol} \quad \text{(opposite leaflet tensions, OLTs).} \tag{18}$$

The OLT states are located on the perpendicular diagonal which is orthogonal to the main diagonal in Fig. 14. All OLT states can be obtained from the reference state by reshuffling lipids from one leaflet to the other, keeping the total lipid number $N_{ll} + N_{ul}$ constant and imposing the constraint of vanishing bilayer tension $\Sigma = \Sigma_{ol} + \Sigma_{il} = 0$. As a consequence, one leaflet is compressed by a negative leaflet tension whereas the other leaflet is stretched by a positive leaflet tension.

The green data in Fig. 14 represent the leaflet tensions arising from changes in the vesicle volume, corresponding to vesicle inflation or deflation (VID). To generate the green VID data, we start again from the reference state with $\Sigma_{il} = \Sigma_{ol} = 0$ but now change the vesicle volume in order to increase or decrease the bilayer tension, thereby mimicking the experimental procedure of osmotic inflation or deflation. It is interesting to note that the green data do not follow the main diagonal. Therefore, during a VID step, both leaflet tensions are changed by different amounts.

3.2.6 Voronoi tessellation and volume per lipid

The VORON protocol, used to obtain the leaflet tensions in Fig. 14, is based on three-dimensional Voronoi tessellation, which assigns a polyhedral cell to each bead (Zamaletdinov et al., 2023). This cell is defined by the requirement that all points in the cell are closer to the center of the chosen bead than to the center of any other bead. The tensionless leaflets obtained via the VORON protocol have essentially the same volume per lipid in both leaflets, irrespective of the size and curvature of the nanovesicles (Zamaletdinov et al., 2023). In contrast, the optimal lipid areas are different for the two leaflets and depend on the vesicle size. In fact, the area per lipid in the inner leaflet is always found to be larger than the area per lipid in the outer leaflet (Ghosh et al., 2019; Sreekumari & Lipowsky, 2022; Zamaletdinov et al., 2023). Thus, for each nanovesicle, the inner leaflet is more loosely packed compared to the outer leaflet. This difference in molecular packing is consistent with the intuitive view that lipids with two hydrocarbon chains prefer to reside in a weakly rather than in a strongly curved surface. Therefore, when these lipids are forced to pack into the more highly curved inner leaflet, they experience an increased "geometric frustration" which leads to a looser molecular packing and to an increased area per lipid.

3.2.7 Stress asymmetry of vesicle bilayers

The stress asymmetry $\Delta\Sigma_{\rm ve}$ between the two leaflet tensions of a vesicle bilayer is defined by (Sreekumari & Lipowsky, 2022; Lipowsky et al., 2023)

$$\Delta\Sigma_{\rm ve} \equiv \Sigma_{ol} - \Sigma_{il} = \int_{r_{\rm mid}}^{r_{\rm max}} {\rm d}r\ s(r) - \int_{0}^{r_{\rm mid}} {\rm d}r\ s(r) \tag{19}$$

where the second equality follows from the integral expressions for the leaflet tensions in Eq. (B1).

The stress asymmetry $\Delta\Sigma$ in Eq. (19) vanishes for all states of the vesicle bilayer with equal leaflet tensions $\Sigma_{il} = \Sigma_{ol}$. However, these equal leaflet tension states are not easy to determine for nanovesicles in terms of the corresponding lipid numbers N_{il} and N_{ol} of the inner and outer leaflets because, in contrast to symmetric planar bilayers, these lipid numbers are not related by any symmetry. Thus, for vesicle bilayers with $N_{il} + N_{ol} = 2525$ as depicted in Fig. 12b, the reference state with tensionless leaflets is obtained for $N_{il} = 840$ lipids in the inner and $N_{ol} = 1685$ lipids in the outer leaflet.

All OLT states of the vesicle bilayer, corresponding to the black data in Fig. 14, exhibit a nonzero stress asymmetry $\Delta\Sigma_{\rm ve}$ because the OLT states are characterized by one stretched and one compressed leaflet. In fact, apart from the equal leaflet tension states along the main diagonal of the two-dimensional leaflet tension space in Fig. 14, all points $(\Sigma_{il}, \Sigma_{ol})$ of this space lead to a nonzero stress asymmetry. Stress asymmetries of planar bilayers have also been studied by Deserno and coworkers (Hossein & Deserno 2020; Foley & Deserno, 2020; Varma & Deserno, 2022), who used the term "differential stress" instead of "stress asymmetry".

4. Instabilities of lipid bilayers

The vesicle bilayers discussed so far experienced moderate leaflet tensions Σ_{ol} and Σ_{il}, see Fig. 13, and thus small stress asymmetries $\Delta\Sigma_{\rm ve} = \Sigma_{ol} - \Sigma_{il}$. In this regime of small $\Delta\Sigma_{\rm ve}$, the phospholipids do not undergo flip-flops on the time scales of the simulations (Ghosh et al., 2019). This stability of the lipid bilayers is no longer observed when we consider an extended range of leaflet tensions and larger stress asymmetries. Indeed, for sufficiently large stress asymmetries, the phospholipids start to undergo flip-flops between the two leaflets and the bilayers exhibit structural instabilities even for vanishing bilayer tension.

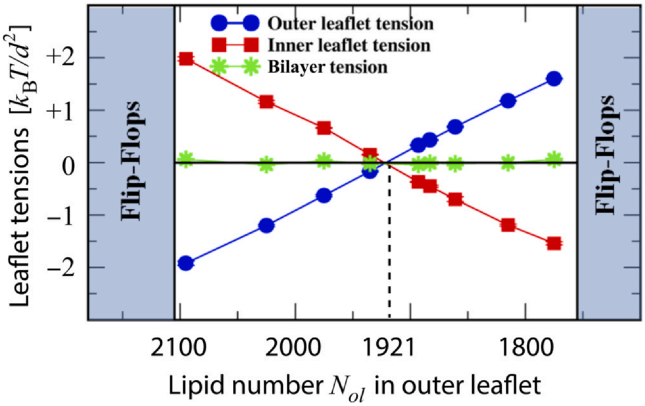

Fig. 15 Stability and instability regimes for nanovesicles assembled for total lipid number $N_{ol} + N_{il} = 2875$. The CHAIN protocol was used to compute the outer leaflet tension Σ_{ol} (blue) and the inner leaflet tension Σ_{il} (red) versus the lipid number N_{ol} in the outer leaflet. Both leaflet tensions vanish for $N_{ol} = 1921$ and $N_{il} = 954$ (vertical dashed line), which defines the relaxed reference state of the nanovesicles. The green data represent the bilayer tension $\Sigma = \Sigma_{ol} + \Sigma_{il}$, which is close to zero. During the run time of 12.5 μs, we observed no flip-flops within the stability regime (white), corresponding to $2095 \geq N_{ol} \geq 1775$. The left vertical line at $N_{ol} = 2105$ represents the instability line at which the lipids start to undergo flip-flops from the compressed outer to the stretched inner leaflet. The right vertical line at $N_{ol} = 1755$ represents the instability line at which the lipids start to undergo flip-flops from the compressed inner to the stretched outer leaflet (Sreekumari & Lipowsky, 2022).

4.1 Stability regime of vesicle bilayers

To illustrate the stability and instability of vesicle bilayers, we consider bilayers that are assembled from a fixed total number of 2875 lipids, with N_{il} lipids in the inner leaflet and $N_{ol} = 2875 - N_{il}$ lipids in the outer leaflet. We adjust the vesicle volume to $\nu = \nu_0$ so that the bilayer tension $\Sigma = \Sigma_{il} + \Sigma_{ol}$ is close to zero. For all simulations described in the present section, the vesicle volume has the value $\nu = \nu_0$. Using the CHAIN protocol for the average position $r = r_{\text{mid}}$ of the leaflet–leaflet interface, we obtain the leaflet tensions Σ_{ol} and Σ_{il} as plotted in Fig. 15 as functions of the lipid number N_{ol} in the outer leaflet.

Inspection of Fig. 15 shows that both leaflet tensions vanish when the outer leaflet contains between 1893 and 1935 lipids. Linear interpolation then leads to tensionless leaflets for $N_{ol} = 1921$ lipids in the outer leaflet and $N_{il} = 954$ lipids in the inner one. Thus, for these nanovesicles, the lipid number in the tensionless outer leaflet is more than twice as large as the one in the tensionless inner leaflet. As a consequence, the area per lipid in the tensionless outer leaflet is smaller than the area per lipid in the tensionless inner leaflet, which implies that the tensionless inner leaflet is more loosely packed than the tensionless outer leaflet.

When we start from the reference state with tensionless leaflets and reshuffle some lipids between these leaflets, we obtain nonzero leaflet tensions Σ_{ol} and Σ_{il}. The two leaflets form bilayers that remain stable for the lipid number range $1775 \leq N_{ol} \leq 2095$ and for the leaflet tension range $1.60\, k_B T/d^2 \leq \Sigma_{ol} \leq -1.94\, k_B T/d^2$, as shown by the white stability regime in Fig. 15. Flip-flops from the compressed inner to the stretched outer leaflet are observed for $N_{ol} \leq 1755$ and $\Sigma_{ol} \geq +1.78\, k_B T/d^2$, corresponding to the right shaded region in Fig. 15. Flip-flops from the compressed outer to the stretched inner leaflet occur for $N_{ol} \geq 2105$ and $\Sigma_{ol} \leq -1.97\, k_B T/d^2$, which defines the left shaded region in Fig. 15. Within these two instability regimes for $N_{ol} < 1755$ and $N_{ol} > 2105$, we also observe structural instabilities of the lipid bilayers in addition to the flip-flops.

4.2 Stress-induced flip-flops of lipids

We now focus on the left instability regime in Fig. 15, corresponding to compressed outer leaflets with $\Sigma_{ol} < 0$ and stretched inner leaflets with $\Sigma_{il} > 0$. Within this instability regime, the lipids undergo flip-flops from the outer to the inner leaflets. To determine the kinetic rates, we examined different ensembles of nanovesicles. Each ensemble consisted of more than 60 vesicles that were initially assembled from the same lipid numbers N_{ol} and N_{il} and, thus, experienced the same leaflet tensions as long as they remained in their initial states. More precisely, the bilayers experienced the same initial leaflet tensions until time t_1, at which the first flip-flop occurred. The statistics of t_1 is described by the cumulative distribution function $P_{\text{cdf}}(t)$ that represents the probability that the first flip-flop occurs at time $t_1 \leq t$. This distribution function is depicted in Fig. 16 for three ensembles of nanovesicles with tensionless bilayers. All bilayers contain the same total lipid number $N_{ol} + N_{il} = 2875$ but differ in the outer lipid number N_{ol}.

The cumulative distribution functions in Fig. 16 have a sigmoidal shape with a point of inflection at intermediate times. This sigmoidal shape is qualitatively different from the exponential distribution that can be used to fit the onset of flip-flops in planar bilayers (Sreekumari & Lipowsky, 2022) Distribution functions with a sigmoidal shape can be obtained by generalizing the exponential distributions to Weibull distributions as provided by (Weibull, 1951)

$$P_{\mathrm{Wei}}(t) = 1 - \exp[-(\omega_{\mathrm{ve}} t)^k], \tag{20}$$

which involve stretched exponentials. The Weibull distributions depend on two parameters, the rate parameter ω_{ve} and the dimensionless shape parameter $k > 0$. For $k = 1$, the Weibull distribution in Eq. (20) becomes identical to the exponential distribution. For $k \neq 1$, the empirical Weibull distribution has been applied to a large variety of different processes (Rinne, 2008; Laim, 2014).

The inset of Fig. 16 shows that the rate parameter ω_{ve} increases monotonically with the absolute value of the stress asymmetry between the two leaflet tensions. This behavior demonstrates that the leaflet tensions and the associated stress asymmetry represent key parameters for the lipid

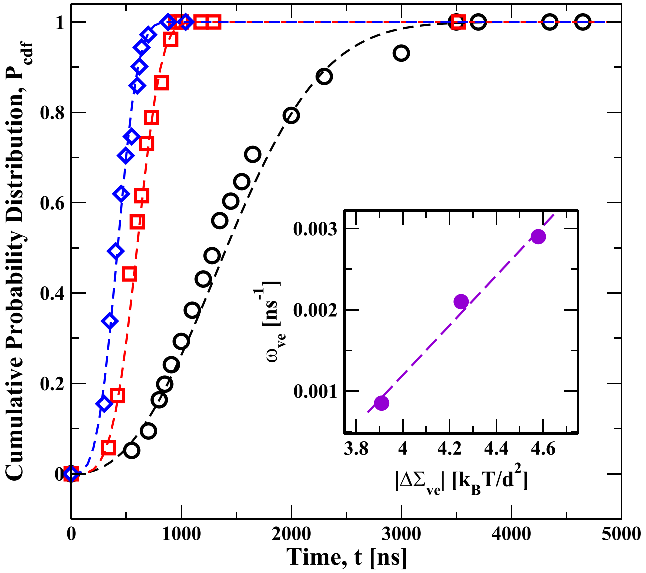

Fig. 16 Cumulative distribution function P_{cdf} for the first flip-flop time t_1 versus time t for tensionless bilayers of nanovesicles, assembled from $N_{ol} + N_{il} = 2875$ lipids. Three sets of data are displayed with $N_{ol} = 2105$ (black circles), $N_{ol} = 2125$ (red squares), and $N_{ol} = 2150$ (blue diamonds) lipids in the outer leaflet, which belong to the left instability regime in Fig. 15. The three sets of data are well fitted, using least squares, to Weibull distributions (broken lines) as in Eq. (20), which depend on two parameters, the shape parameter k and the rate parameter ω_{ve}. Each data set represents the outcome of at least 70 statistically independent simulations. Inset: Monotonic increase of the rate parameter ω_{ve} with the absolute value $|\Delta\Sigma_{\mathrm{ve}}|$ of the stress asymmetry as defined by Eq. (19) (Sreekumari & Lipowsky, 2022).

flip-flops between the two bilayer leaflets. The dashed curves in Fig. 16 represent the best fits to the three data sets as obtained for $N_{ol} = 2105$, 2125, and 2150. The rate parameters ω_{ve} obtained from these fits are displayed in the inset of Fig. 16, the shape parameters k corresponding to these fits are $k = 2.39$, 3.92, and 3.33. (Sreekumari & Lipowsky, 2022). Because $k > 1$, the instantaneous flip-flop rate increases with the age of the metastable state. In mathematical statistics, the instantaneous rate is known as the hazard rate and equal to the ratio of the probability density function $\mathrm{d}P_{\mathrm{cdf}}/\mathrm{d}t$ to the survival probability $1 - P_{\mathrm{cdf}}(t)$ (Cox, 1962; Taylor & Karlin, 1998). The only distribution that leads to a constant and age-independent hazard rate is the exponential distribution. Therefore, the sigmoidal shape of the cumulative distribution functions as displayed in Fig. 16 implies ageing of the metastable bilayer states.

4.3 Stress-induced structural instabilities

In addition to the flip-flops, the instability regimes in Fig. 15 lead to structural instabilities followed by self-healing of the bilayers. One example is displayed in Fig. 17 which corresponds to the left instability regime in Fig. 15, characterized by a compressed outer and a stretched inner leaflet. The vesicle bilayer in Fig. 17 is initially assembled from $N_{ol} = 2105$ lipids in the outer and $N_{il} = 770$ lipids in the inner leaflet. After adjusting the vesicle volume to obtain a tensionless bilayer, the outer leaflet is compressed by the negative leaflet tension $\Sigma_{ol} = -1.97\, k_{\mathrm{B}}T/d^2$ whereas the inner leaflet is stretched by the positive leaflet tension $\Sigma_{il} = 1.94\, k_{\mathrm{B}}T/d^2$.

During the first 1300 ns, the bilayer of the nanovesicle in Fig. 17a undergoes shape fluctuations that appear to be 'normal' until the outer leaflet starts to develop a protrusion by expelling some lipids. This protrusion grows rapidly into a cylindrical micelle, which reaches its maximal extension after 1720 ns as shown in Fig. 17b. Somewhat later, some lipids move into the inner leaflet, primarily along the contact line between the micelle and the bilayer, see snapshot at 2160 ns in Fig. 17c. This lipid exchange decreases the number of lipids within the compressed outer leaflet and increases the number of lipids within the stretched inner leaflet until 111 red-green lipids have been moved from the outer to the inner leaflet and the ordered bilayer structure has been restored at 2710 ns as shown in Fig. 17d. After this time point, the restored bilayer undergoes no further flip-flops until the end of the simulations. This absence of flip-flops is consistent with the lipid number $N_{ol} = 1994$ in the outer leaflet of the restored bilayer, which belongs to the stability regime in Fig. 15.

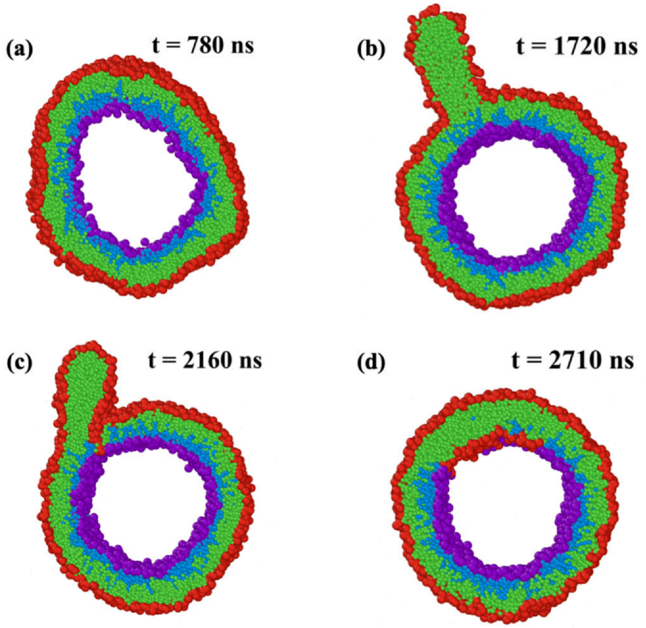

Fig. 17 Stress-induced instability of a vesicle bilayer that consists of $N_{ol} + N_{il} = 2875$ lipids in both leaflets. At time $t = 0$, the bilayer is assembled from $N_{ol} = 2105$ and $N_{il} = 770$ lipids and the vesicle volume is adjusted in such a way that the bilayer tension is close to zero, which leads to a compressed outer leaflet with negative leaflet tension $\Sigma_{ol} = -1.97\ k_B T/d^2$: (a) At $t = 780$ ns, the compressed outer leaflet leads to some kinky bilayer deformations; (b) At $t = 1720$ ns, a cylindrical micelle has been formed from about 180 red-green lipids that were expelled from the outer leaflet; (c) At $t = 2160$ ns, lipids move towards the stretched inner leaflet along the contact line between micelle and bilayer; and (d) At $t = 2710$ ns, the self-healing process via stress-induced lipid exchange has been completed and 111 red-green lipids have moved to the inner leaflet. The restored bilayer undergoes no further flip-flops until the end of the simulations (Sreekumari & Lipowsky, 2022).

5. Remodeling of vesicle topology

5.1 Topology of closed vesicle membranes

The closed membrane surface of a giant vesicle separates the interior vesicle compartment from the exterior space. In general, the topology of any closed surface in three dimensions can be characterized by two equivalent integers: (i) the Euler characteristic χ and (ii) the number $\mathfrak{g}$ of handles or loops formed by this surface. The integer number $\mathfrak{g}$ defines the topological genus of the surface.

5.1.1 Euler characteristic

The Euler characteristic of a closed membrane surface can be obtained from any partitioning of the surface into a discrete set of surface segments (do Carmo, 1976). One widely applied discretization method is triangulation but one may also use a mesh of smooth curves that are embedded in the surface. Any discretization involves the surface segments themselves, usually called 'faces', the edges between neighboring faces, and the vertices at which several edges come together. Counting the number of faces, F, the number of edges, E, and the number of vertices, V, the Euler charactersitic χ is obtained via

$$\chi = F - E + V. \tag{21}$$

The three numbers F, E, and V depend on the chosen partitioning of the surface, as one can easily see by using different polyhedra to discretize a sphere. In contrast, the Euler characteristic χ itself is independent of this partitioning and defines the topology of the surface. Thus, we obtain $\chi = 2$ for a tetrahedron, a cube or an icosahedron as well as for any other partitioning of the spherical surface. The torus or doughnut surface has the Euler characteristic $\chi = 0$, the double-torus or button surface has $\chi = -2$, and the combined surface of N_{ve} spherical vesicles is characterized by $\chi = 2N_{\text{ve}}$.

5.1.2 Topological genus

The number $\mathfrak{g}$ of handles or loops provides another, equivalent characterization of a closed membrane surface, the so-called topological genus $\mathfrak{g}$, which satisfies

$$\mathfrak{g} = 1 - \frac{1}{2}\chi \quad \text{and} \quad \Delta\mathfrak{g} = -\frac{1}{2}\Delta\chi \tag{22}$$

where $\Delta\mathfrak{g} \equiv \mathfrak{g}_2 - \mathfrak{g}_1$ is the difference between the genera of two surfaces 1 and 2, which is equal to minus half the difference $\Delta\chi \equiv \chi_2 - \chi_1$ between the Euler characteristics of the two surfaces. For a sphere and a torus, the topological genus is equal to $\mathfrak{g} = 0$ and $\mathfrak{g} = 1$, respectively. Positive values of the topological genus $\mathfrak{g}$ can be deduced directly from the global surface geometry by counting the number of handles or loops formed by the surface, without any partitioning or discretization of this surface. Furthermore, the linear relation between $\mathfrak{g}$ and χ as given by Eq. (22) can be used to define negative values of the topological genus $\mathfrak{g}$, as obtained for $N \geq 2$ vesicles with $\chi \geq 2N$. Likewise, this relation leads to negative values of the Euler characteristic χ for $\mathfrak{g} \geq 2$.

5.2 Topological transformations of vesicles

By definition, a topological transformation of a vesicle or another closed membrane compartment implies that this compartment changes its topology and, thus, its Euler characteristic and topological genus. In the living cell, the membrane-bound organelles continuously undergo such topological transformations by membrane fission and membrane fusion. The fission and fusion processes of intracellular membranes can be mimicked by the fission and fusion of giant vesicles, which demonstrates that individual fission and fusion events proceed via localized perturbations of the vesicle membranes.

5.2.1 *Local topology changes by fission and fusion*

Different vesicle topologies can be transformed into each other by individual fusion and fission processes. The intermediate transition states between the different topologies involve closed membrane necks as depicted in Fig. 3. These necks are cleaved by fission and created by fusion. Therefore, individual fission and fusion events proceed via some 'local surgery' which can be characterized by the change $\Delta\chi$ in the Euler characteristic or, equivalently, by the change $\Delta\mathfrak{g}$ in the topological genus, without knowing the global shape and topology of the membrane compartment.

A single, local *fission* event leads to an increase of the Euler characteristic by $\Delta\chi = +2$ and to a decrease of the topological genus by $\Delta\mathfrak{g} = -\frac{1}{2}\Delta\chi = -1$. On the other hand, a single, local *fusion* event leads to a decrease of the Euler characteristic by $\Delta\chi = -2$ and to an increase of the genus by $\Delta\mathfrak{g} = +1$. These positive and negative values of $\Delta\chi$ and $\Delta\mathfrak{g}$ for single fission and fusion events are completely general and apply to any shape and topology of the membrane compartment as long as this compartment forms a closed surface without bilayer pores or bilayer edges, both before and after such an event.

5.2.2 *Fission geometries for two-sphere vesicles*

Two-sphere vesicles provide simple and instructive examples for vesicles with closed membrane necks and topological genus $\mathfrak{g} = 0$. As shown in Fig. 3, two-sphere vesicles can exhibit two different geometries corresponding to out-budded and in-budded vesicle shapes. An out-budded or positive two-sphere shape as in Fig. 3a has a positive membrane neck with neck curvature $M_{ls}^{\mathrm{eff}} > 0$, see Eq. (10), which can be formed for positive spontaneous curvature $m \geq M_{ij}^{\mathrm{eff}}$ as in Eq. (12). An in-budded or negative two-sphere shape as in Fig. 3b has a negative membrane neck with neck curvature $M_{ls}^{\text{eff}} < 0$, see Eq. (11), which can be formed for negative spontaneous curvature $m \leq M_{ij}^{\text{eff}}$ as in Eq. (13).

For both geometries, the fission process is completed by the cleavage of the membrane neck. After the neck cleavage of an out-bud, the newly created daughter vesicle is released into the exterior space. In contrast, the cleavage of an in-bud leads to an intraluminal daughter vesicle within the interior compartment of the mother vesicle. The out-budded vesicle in Fig. 3a and the in-budded vesicle in Fig. 3c have the same Euler characteristic $\chi = 2$ and the same topological genus $\mathfrak{g} = 0$. After neck fission, the two daughter vesicles are characterized by $\chi = 4$ and $\mathfrak{g} = -1$, both for the release of the out-bud into the exterior space and for the release of the in-bud into the interior vesicle compartment.

Thus, the two fission processes for out-budded and in-budded vesicles lead to the same topological changes but one should note one difference between these two processes, related to the mean curvatures of the two daughter vesicles. For the fission of an out-budded vesicle, each daughter vesicle has a positive mean curvature, which implies that both mean curvatures are stabilized by the positive spontaneous curvature of the vesicles. In contrast, for the fission of an in-budded vesicle, the smaller daughter vesicle has a negative mean curvature whereas the larger daughter vesicle has a positive mean curvature, the latter being antagonistic to the negative spontaneous curvature of the membrane.

5.2.3 Fusion geometries for spherical vesicles

Next, let us consider the fusion of two spherical vesicles with Euler characteristic $\chi = 4$ and topological genus $\mathfrak{g} = -1$. When the two vesicles enclose two different spatial regions, the fusion process leads to a two-sphere vesicle as in Fig. 3a,b with a positive membrane neck. On the other hand, when we start from two nested vesicles, fusion leads to an in-budded two-sphere vesicle with a negative membrane neck as in Fig. 3c,d. The open necks generated by fusion are traditionally called fusion pores. Thus, the 1-vesicle state obtained after the fusion of two spherical vesicles is identical with a two-sphere vesicle before the fission of its membrane neck. Therefore, as long as we focus on the initial and final states of fusion and fission, the fusion process is the reverse of the fission process.

5.3 Free energy landscapes for fission and fusion

On molecular scales, both the fission of a membrane neck and the formation of such a neck via fusion involve a strong local reorganization of the lipid molecules close to these necks. This molecular reorganization will determine the free energy barriers for the fission and fusion processes as schematically displayed in Fig. 18. For fission, this barrier must be overcome by the constriction force f acting against the neck.

5.3.1 Free energy landscape for fission

The process of neck fission and vesicle division transforms the 1-vesicle state provided by the dumbbell or two-sphere shape to the 2-vesicle state of two separate daughter vesicles as shown in the schematic free energy landscape of Fig. 18a (Steinkühler et al., 2020). Similar schemes for the free energy landscape of fission have been displayed in Refs Lipowsky (2018b) and Deserno (2018). The two states before and after fission have essentially the same bending energy because the closed neck of the two-sphere shape does not contribute to this energy. However, the two states have different topologies which implies that the Gaussian curvature term, which is equal to $2\pi\chi\kappa_G$ according to Eq. (2), makes a different contribution to the 1-vesicle and to the 2-vesicle state. Indeed, the Gaussian curvature term is

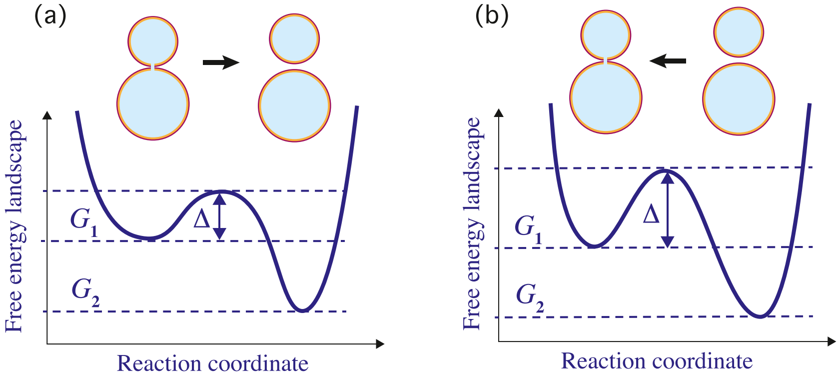

Fig. 18 Free energy landscapes for individual fission and fusion events: Schematic landscape for an exergonic (or downhill) fission process in (a) and for an endergonic (or uphill) fusion process in (b). The free energy G_2 of the 2-vesicle state is lower than the free energy G_1 of the 1-vesicle state. The negative free energy difference $G_2 - G_1 < 0$ implies that the exergonic fission process can proceed spontaneously whereas the endergonic fusion process must be coupled to another exergonic process such as nucleotide hydrolysis. The kinetics of these processes is governed by the free energy barriers Δ.

equal to $4\pi\kappa_G$ for the 1-vesicle state with $\chi = 2$ and to $8\pi\kappa_G$ for the 2-vesicle state with $\chi = 4$. Therefore, the difference in free energy, $G_2 - G_1$, between the 2- and the 1-vesicle state is equal to $4\pi\kappa_G$. Furthermore, both experimental studies (Derzhanski et al., 1978; Lorenzen et al., 1986) and computer simulations (Briguglio et al., 2012) indicate that the Gaussian curvature modulus κ_G is negative and can be estimated by the negative bending rigidity κ, that is, by $\kappa_G \simeq -\kappa$. For a lipid bilayer, the bending rigidity has the typical value $\kappa \simeq 10^{-19} J \simeq 20\, k_B T$ at room temperature which leads to the free energy difference $G_2 - G_1 \simeq -4\pi\kappa \simeq -250\, k_B T$. Therefore, neck fission and GUV division is a strongly exergonic process and can, in principle, occur spontaneously. However, the rate, with which this process proceeds, is governed by the free energy barrier that separates the 1-vesicle from the 2-vesicle state.

5.3.2 Free energy barrier for neck fission

A simple estimate for the free energy barrier, which has to be overcome by the fission process, can be obtained as follows. In order to cleave the neck, we have to create two bilayer pores with a radius that is comparable to the radius $R_{ne} \simeq 2\ell_{me}$ of the closed membrane neck before fission where ℓ_{me} is the thickness of the bilayer membrane. The resulting free energy barrier is governed by the bilayer edges of these two pores. The associated edge free energy is equal to the edge tension λ_{ed} times the combined circumference $4\pi R_{ne}$ of the two pores, which leads to the estimate $4\pi R_{ne}\lambda_{ed}$ for the free energy barrier. To overcome this barrier, the constriction force f acting against the closed neck must expend mechanical work of the order of fR_{ne}, thereby decreasing the radius of the neck from $R_{ne} \simeq \ell_{me}$ to $R_{ne} = 0$ (Lipowsky, 2019). For a positive neck as displayed in Fig. 18, the curvature-induced constriction force is equal to $f = 8\pi\kappa\,(m - M_{ne}^{eff})$ as given by Eq. (14). It then follows from

$$fR_{ne} = 8\pi\kappa\,(m - M_{ne}^{eff})R_{ne} \gtrsim 4\pi R_{ne}\lambda_{ed} \tag{23}$$

that the neck undergoes fission if the spontaneous curvature exceeds the value $\lambda_{ed}/(2\kappa)$. The edge tension λ_{ed} is expected to be reduced by the constriction force, which pushes against the neck and leads to a local thinning of the lipid bilayer close to the neck.

5.3.3 Free energy landscape for fusion

Now, consider the fusion of two spherical vesicles as in Fig. 18b. For simplicity, we take the two vesicles to have the same molecular composition before fusion which implies that this composition also applies to the resulting 1-vesicle state after fusion. Because the curvature-elastic parameters are determined by the molecular composition, the 1-vesicle state after fusion has the same curvature-elastic parameters as the two vesicles before fusion. It then follows that the 1-vesicle state has the same bending energy as the 2-vesicle state, where we ignore the small contribution from the fusion neck (or pore) after fusion. Therefore, the free energy difference $G_2 - G_1$ is again determined by the Gaussian curvature modulus κ_G and can again be estimated by $G_2 - G_1 \simeq 4\pi\kappa_G \simeq -4\pi\kappa$, which leads to the same free energy difference $G_2 - G_1 \simeq -250\, k_B T$ for $\kappa \simeq 20\, k_B T$ as for the fission process. Furthermore, because the free energy G_1 of the 1-vesicle state after fusion is much larger than the free energy G_2 of the two vesicles before fusion. we can immediately conclude that the fusion process is endergonic (or uphill) and is unlikely to occur spontaneously, in contrast to the fission process.

The free energy barrier for fusion has to be overcome by attractive interactions that lead to the adhesion of the two membranes to be fused. These attractive interactions must in particular overcome the strong repulsive forces arising from the hydration of the lipid bilayers. In the cell, these attractive interactions are typically provided by some protein machinery, which acts to generate a local contact between the two membranes. Thus, from our point of view, the main distinction between fission and fusion is that the fusion process requires membrane adhesion whereas the fission process does not. A different point of view about this distinction has been described in Ref. Deserno (2018).

5.4 Neck fission and division of giant vesicles

The controlled division of GUVs has been recently achieved by binding His-tagged GFP to anchor lipids in the GUV membranes (Steinkühler et al., 2020). As explained in Section 2.3, membrane-bound GFP generates a significant spontaneous curvature as described by Eq. (16). Furthermore, a positive membrane neck as in Fig. 19a experiences a large curvature-dependent constriction force $f_{\mathrm{pos}} = 8\pi\kappa\,(m - M_{\mathrm{ne}}^{\mathrm{eff}})$ as given by Eq. (14) and displayed in Fig. 19b for the measured bending rigidity $\kappa \simeq 48\, k_B T$ (Steinkühler et al., 2020).

As shown in Fig. 19b, membrane-bound GFP generates constriction forces up to 80 pN, comparable to the largest constriction forces generated by specialized protein complexes that cleave the necks of cellular membranes. Therefore, the cleavage of membrane necks and the concomitant

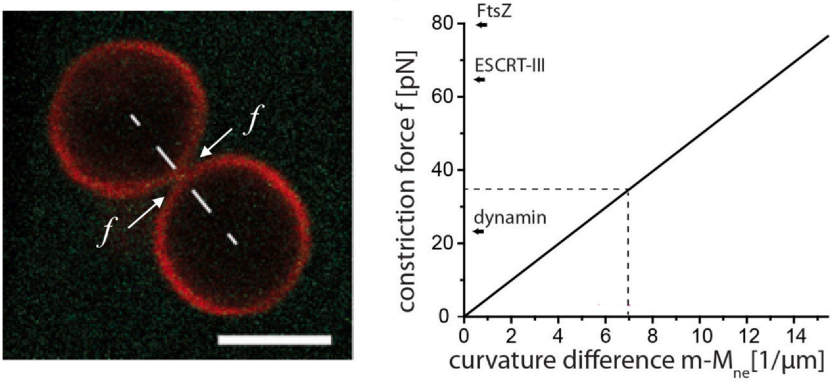

(a)

(b)

Fig. 19 Curvature-induced constriction force $f = f_{pos}$ compressing the closed membrane neck of a giant vesicle: (a) Confocal image of a vesicle (red) that consists of two equally sized spheres connected by a closed neck. The spontaneous curvature is generated by His-tagged GFP which binds to the membrane from the exterior solution. Scale bar: 5 μm; and (b) Constriction force f as a function of the excess curvature $m - M_{ne}$. The straight line corresponds to Eq. (14) with $\kappa = 48\, k_B T$. The dashed lines represent the values of $m - M_{ne}$ and f for the membrane neck in (a). For comparison, the plot also includes literature values for the constriction forces as generated by the specialized protein complexes of dynamin (Roux et al., 2010), ESCRT-III (Schoeneberg et al., 2018), and FtsZ (Xiao & Goley, 2016). Thus, the curvature-induced constriction force in (a) lies within the range of force values found in vivo (Steinkühler et al., 2020).

division of GUVs can be induced simply by an increase in the GFP solution concentration X and the resulting spontaneous curvature as given by Eq. (16) (Steinkühler et al., 2020).

The controlled division process consists of three steps. First, the volume of the GUV is adjusted by osmotic deflation or inflation to attain an appropriate value for the volume-to-area ratio v. Second, the GFP concentration in the exterior solution is increased until the GUV attains a two-sphere shape with a closed membrane neck. Third, increasing the GFP concentration even further leads to the cleavage of the neck and to the division of the GUV.

5.5 Neck fission and division of nanovesicles

The deflation of a spherical nanovesicle with $N_{ol} = 5700$ lipids in the outer leaflet and $N_{il} = 4400$ lipids in the inner leaflet leads to a stomatocyte shape with an open membrane neck as shown in Fig. 11. By reshuffling 200 lipids from the outer to the inner leaflet, we obtain a new initial vesicle state with

$N_{ol} = 5500$, which transforms into a stomatocyte shape with a closed neck that undergoes membrane fission within about 15 μs as shown in Fig. 20. As a result of this fission process, the vesicle is divided up into two nested daughter vesicles, which adhere to each other.

The two leaflets of the vesicle displayed in Fig. 20 contain $N_{ol} + N_{il} = 10100$ lipids, which is the same total lipid number as for the vesicles in Figs. 10 and 11. Therefore, the leaflet tensions for the spherical vesicle in the first panel of Fig. 20 can be estimated by extrapolation of the leaflet tension data in Fig. 13b. This extrapolation leads to a stretched outer leaflet with $\Sigma_{ol} = 1.485\, k_B T/d^2$ and to a compressed inner leaflet with $\Sigma_{il} = -1.44\, k_B T/d^2$, which implies the stress asymmetry $\Delta\Sigma_{\text{ve}} = 2.9\, k_B T/d^2$. These leaflet tensions belong to the stability regime for the lipid bilayer of the smaller nanovesicle with $N_{ol} + N_{il} = 2875$ lipids as follows from Fig. 15.

The diameter of a spherical nanovesicle can be estimated from the mean value of the diameters for the two headgroup layers. For total lipid number $N_{ol} + N_{il} = 10100$ and vanishing bilayer tension as in Fig. 20, the spherical nanovesicle has a diameter of about 44 d or 35 nm (Ghosh et al., 2019). For total lipid number $N_{ol} + N_{il} = 2875$ and vanishing bilayer tension as in Fig. 14, the nanovesicle has a diameter of about 23.4 d or 18.7 nm. For such a small nanovesicle, it seems difficult to accommodate an in-bud when the vesicle volume is reduced but the latter process remains to be investigated.

Fission of nanovesicles can be facilitated by several molecular mechanisms as observed in other simulation studies. These mechanisms include complete engulfment of nanoparticles (Noguchi & Takasu, 2002),

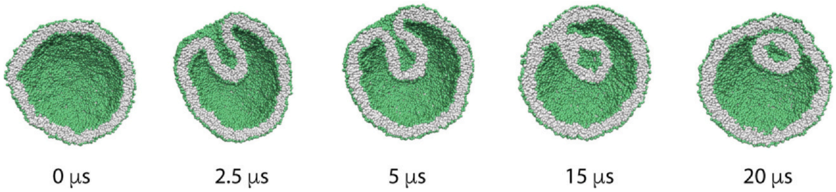

Fig. 20 Time-lapse snapshots for the division of a nanovesicle with $N_{ol} = 5500$ lipids in the outer and $N_{il} = 4600$ lipids in the inner leaflet, corresponding to a stretched outer leaflet and a compressed inner leaflet with bilayer tension $\Sigma = \Sigma_{ol} + \Sigma_{il}$ close to zero. Until time $t = 0$ μs, the vesicle has a spherical shape with a certain volume as determined by the number of water molecules within the interior vesicle compartment. At $t = 0$ μs, the vesicle volume is reduced by 20%. After this volume reduction, the vesicle develops an in-bud with a membrane neck that is closed at $t = 5$ μs. At about $t = 15$ μs, the neck undergoes fission, thereby generating an intraluminal daughter vesicle that adheres to the inner leaflet of the larger daughter vesicle (Lipowsky et al., 2023b).

two-domain vesicles with the domain boundary being located in the membrane neck (Urakami et al., 2018; Li et al., 2009), protein helices mimicking dynamin (Pannuzzo et al., 2018), and the adsorption of small solutes onto the outer leaflet of the nanovesicle (Ghosh et al., 2021).

5.6 Droplet endocytosis by nanovesicles

For phase-separated PEG-dextran solutions within giant vesicles as in Fig. 7c and d, the formation of two spherical subcompartments has been observed, with one subcompartment enclosing the PEG-rich α droplet whereas the other subcompartment was filled with the dextran-rich β droplet, but these two vesicles remained connected by a membrane nanotube (or tether) (Andes-Koback & Keating, 2011; Dimova & Lipowsky, 2017). Thus, for giant vesicles, a closed membrane neck as in Fig. 7 has not yet been reported to undergo fission. This neck fission represents, however, a necessary step for the endo- and exocytosis of condensate droplets. Therefore, neither endo- nor exocytosis have been observed, so far, for giant vesicles. In contrast, the adhesion of small droplets to nanovesicles can lead to the endocytosis of these droplets as demonstrated by molecular dynamics simulations and described in the following paragraphs.

5.6.1 Adhesion of condensate droplets to nanovesicles

The adhesion of a small condensate droplet to a nanovesicle as observed in molecular dynamics simulations is shown in Fig. 21. The adhesion geometry involves again three liquid phases as in Fig. 6a: the two coexisting phases α and β in the exterior solution as well as the inert spectator phase γ within the interior vesicle compartment. After the onset of adhesion, the droplet starts to spread over the membrane as in Fig. 21b, which leads to partial engulfment of the droplet by the membrane as in Fig. 21c. The contact area of droplet and membrane defines the $\beta\gamma$ segment of the membrane while the membrane segment exposed to the α phase represents the $\alpha\gamma$ segment. The size of the $\beta\gamma$ segment depends on the relative size of droplet and vesicle.

5.6.2 Partial versus complete engulfment

During the partial engulfment process displayed in Fig. 21, the vesicle volume is kept constant and the contact area of the $\beta\gamma$ segment grows by pulling out excess membrane area that is stored in the thermally-excited shape fluctuations of the membrane. For a further increase of the contact area beyond the value in Fig. 21c, one has to reduce the vesicle volume, which is filled with the blue γ phase. Such a volume reduction leads to complete engulfment of the droplet by the vesicle membrane, provided the droplet volume is sufficiently small compared to the vesicle volume, which applies to Fig. 21c. For a completely engulfed droplet, the area of the membrane segment $\beta\gamma$ in contact with the droplet is equal to the surface area of the droplet and the $\alpha\beta$ interface between the α phase and the β droplet has been replaced by a closed membrane neck, see side views in Figs. 22 and 23 below.

If the droplet is too large, complete engulfment is not possible without membrane rupture (Lipowsky, 2019; Ghosh et al., 2023). This geometric constraint is obvious from an intuitive point of view and can be described in a quantitative manner using the isoperimetric inequality (Osserman, 1978; Hildebrandt & Tromba, 1985; Ghosh et al., 2023; Lipowsky, 2023). In what follows, we will assume that the droplet is sufficiently small, so that it can be completely engulfed by the vesicle membrane after an appropriate reduction of vesicle volume.

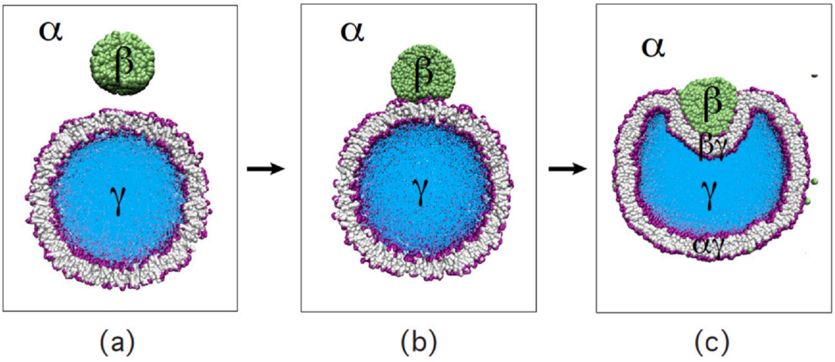

Fig. 21 Partial engulfment of a condensate droplet (green) by the lipid bilayer (purple-grey) of a nanovesicle. The vesicle encloses the aqueous spectator phase γ (blue). Both the nanodroplet and the nanovesicle are immersed in the aqueous bulk phase α (white): (a) Initially, the droplet is well separated from the vesicle which implies that the outer leaflet of the bilayer is only in contact with the α phase; (b) When the droplet is attracted towards the vesicle, it spreads onto the lipid bilayer, thereby increasing its contact area with the vesicle bilayer; and (c) Partial engulfment of the droplet by the membrane after the vesicle-droplet system has relaxed to a new stable state. The contact area between bilayer and β droplet defines the $\beta\gamma$ segment of the bilayer membrane whereas the rest of the bilayer represents the $\alpha\gamma$ segment still exposed to the α phase (Ghosh et al., 2023).

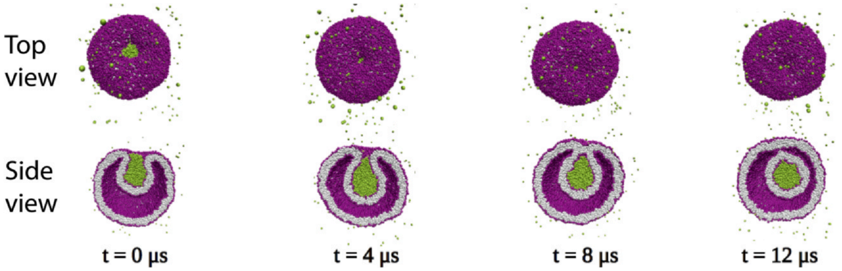

Fig. 22 Endocytosis of condensate droplet (green) via axisymmetric engulfment, followed by the division of the nanovesicle (purple-grey) into two nested daughter vesicles: At time $t = 0$, the droplet is partially engulfed by the vesicle membrane, which forms an open membrane neck. At $t = 4$ μs, the neck closes and the droplet becomes completely engulfed. The neck undergoes fission at $t = 9$ μs, generating a small intraluminal vesicle around the droplet. The vesicle membrane contains $N_{ol} = 5500$ lipids in its outer and $N_{il} = 4600$ lipids in its inner leaflet. The vesicle volume is equal to $v = 0.6$ during the whole endocytic process (Ghosh et al., 2023).

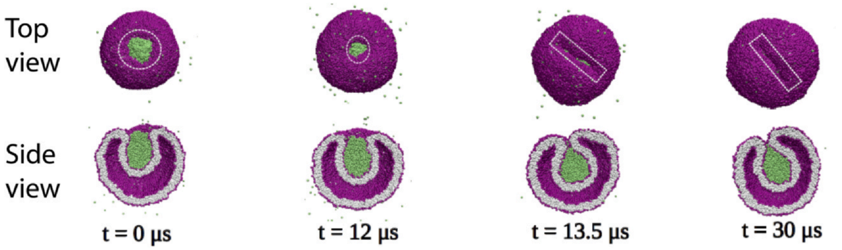

Fig. 23 Non-axisymmetric engulfment of condensate droplet (green), which leads to a tight-lipped shape of the membrane neck that prevents neck fission: Vesicle bilayer (purple-grey) with $N_{ol} = 5700$ lipids in its outer and $N_{il} = 4400$ lipids in its inner leaflet. From $t = 0\ \mu$s until $t = 12\ \mu$s, the vesicle and the partially engulfed droplet are both axisymmetric, see white dashed circles. At $t = 12\ \mu$s, the vesicle volume is reduced from $v = 0.7$ to $v = 0.6$, which leads to complete engulfment of the droplet with a strongly non-circular and highly elongated contact line, see white dashed rectangles in the top views for $t = 13.5\ \mu$s and $t = 30\ \mu$s (Ghosh et al., 2023).

5.6.3 Two-step process of endocytosis

During endocytosis, the condensate droplet originates from the exterior solution as in Fig. 21a and is eventually transferred to the interior vesicle compartment. This endocytic process consists of two steps. First, the droplet is completely engulfed by the membrane, leading to a closed membrane neck that connects the droplet-bound membrane segment to the membrane segment not in contact with the droplet. Complete engulfment is typically induced by the reduction of the vesicle volume and the concomitant release of excess membrane area. The second step of endocytosis is provided by the fission of the closed membrane neck and the division of the vesicle into two daughter vesicles, one of which encloses the droplet.

5.6.4 Two pathways for complete engulfment

Molecular dynamics simulations have demonstrated that the complete engulfment of a condensate droplet can proceed via two different pathways that involve axisymmetric and non-axisymmetric membrane shapes (Ghosh et al., 2023). The axisymmetric pathway leads to a circular contact line between droplet and membrane as well as to a closed membrane neck that undergoes fission, thereby dividing the nanovesicle up into two daughter vesicles, see the simulation snapshots in Fig. 22. In contrast, the non-axisymmetric pathway leads to a strongly non-circular contact line and to a tight-lipped shape of the closed membrane neck, which prevents the fission of this neck, see the simulation snapshots in Fig. 23. Such a tight-lipped membrane neck was first observed in molecular dynamics simulations for complete engulfment of a condensate droplet by a planar bilayer (Satarifard et al., 2018).

5.6.5 Axisymmetric droplet engulfment and endocytosis

The axisymmetric pathway of complete engulfment, which leads to droplet endocytosis, is illustrated by the simulation snapshots in Fig. 22. During this pathway, the contact line between droplet and membrane remains, on average, circular during the whole engulfment process. At the same time, the membrane segment in the vicinity of the contact line develops an axisymmetric membrane neck. The waistline of this neck is identical with the contact line. Both the contact line and the membrane neck become closed after the complete engulfment of the droplet, see the simulation snapshot at time $t = 4\,\mu s$ in Fig. 22. This closed neck undergoes fission, which drives the division of the vesicle into two daugther vesicles, one of which encloses the condensate droplet, see last simulation snapshot in Fig. 22.

5.6.6 Tight-lipped membrane neck and blocked fission

The non-axisymmetric pathway for complete engulfment, which leads to a tight-lipped membrane neck, is illustrated by the simulation snapshots in Fig. 23. In this example, the vesicle volume has the initial value $\nu = 0.7$ until time $t = 12\,\mu s$. During this time period, the contact line between droplet and membrane has a circular average shape, as indicated by the white dashed circles in the first two panels of the upper row in Fig. 23. At $t = 12\ \mu$s, the volume is reduced from $\nu = 0.7$ to $\nu = 0.6$, after which the contact line assumes a strongly non-circular and highly elongated shape, as indicated by the white dashed rectangles in the last two panels of the upper row in Fig. 23. The droplet is again completely engulfed but the membrane neck around the non-circular contact line now attains a tight-lipped shape, which prevents the fission of this neck, see the last panel in the lower row of Fig. 23.

5.6.7 Positive and negative line tension of contact line

The different pathways for complete engulfment and droplet endocytosis are intimately related to the line tension $\lambda_{\rm cl}$ of the contact line between droplet and vesicle membrane. This line tension is plotted in Fig. 24a versus the lipid number N_{ol} in the outer leaflet of the nanovesicles. Inspection of this figure shows that the contact line tension is positive for $N_{ol} = 5400$ and 5500 but negative for $N_{ol} = 5700$ and 5963. Interpolation of these simulation data leads to an estimate for the threshold value $N_{ol}^{[0]}$, at which the line tension changes sign. This threshold value depends weakly on the droplet diameter $D_{\rm dr}$ and varies from $N_{ol}^{[0]} = 5582$ for the smallest

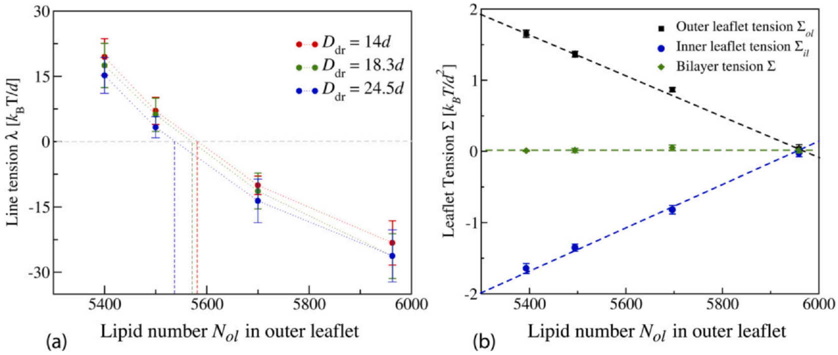

Fig. 24 (a) Line tension $\lambda = \lambda_{\rm cl}$ of the droplet-vesicle contact line versus lipid number N_{ol} in the outer leaflet of the nanovesicles, for droplets with three different diameters $D_{\rm dr}$, see inset. As we increase N_{ol}, the line tension undergoes a transition from positive to negative values. The line tension is positive for $N_{ol} = 5400$ and 5500, for which the whole engulfment process remains axisymmetric as in Fig. 22. On the other hand, for $N_{ol} = 5700$ and 5963, the line tension has a negative value and leads to the formation of a tight-lipped membrane neck as in Fig. 23; and (b) Leaflet tensions Σ_{il} and Σ_{ol} for the inner and outer bilayer leaflets of spherical vesicles with tensionless bilayers as functions of the lipid number N_{ol} (Ghosh et al., 2023).

droplets with a diameter of 11.2 nm to $N_{ol}^{[0]} = 5538$ for the largest droplets with a diameter of 19.6 nm.

For comparison, the simulation data for the two leaflet tensions are displayed in Fig. 24b. These data are obtained for the spherical nanovesicles in the absence of adhering droplets. Furthermore, the green data points for the bilayer tension $\Sigma = \Sigma_{ol} + \Sigma_{il}$ demonstrate that these data are obtained for OLT states with vanishing bilayer tension, $\Sigma_{ol} + \Sigma_{il} = 0$. Inspection of the black and red data for the outer and inner leaflets shows that all spherical vesicles studied here have a stretched outer leaflet with $\Sigma_{ol} > 0$ and a compressed inner leaflet with $\Sigma_{il} < 0$.

It follows from the N_{ol}-dependence of the leaflet tensions in Fig. 24b and from the N_{ol}-dependence of the line tension in Fig. 24a that the line tension λ is positive for large stress asymmetries $\Delta\Sigma_{\text{ve}} = \Sigma_{ol} - \Sigma_{il}$ but negative for small stress asymmetries. This conclusion agrees with the results for symmetric planar bilayers (Satarifard et al., 2018) because the adhesion of condensate droplets to such bilayers leads to a negative line tension as well. As a consequence, the sign of the contact line tension is also controlled by the stress asymmetry between the two leaflet tensions.

5.7 Fusion of nanovesicles

Two nanovesicles that come into close proximity may adhere to each other and undergo fusion. This adhesion and fusion behavior is also controlled by the lipid numbers assembled in the two leaflets and by the associated leaflet tensions. As a simple example, consider two identical vesicles, both of which are characterized by tensionless bilayers with $\Sigma = 0$ as well as by stretched outer and compressed inner leaflets with $\Sigma_{ol} > 0$ and $\Sigma_{il} < 0$ before they come into contact. The vesicles start to adhere to each other but may then attain a stable adhesive state or undergo fusion, depending on the magnitude of the leaflet tensions (Lipowsky et al., 2023).

For $N_{ol} = 5700$ lipids in the outer and $N_{il} = 4400$ lipids in the inner leaflets of the vesicle bilayer, the inner leaflets are compressed by the negative leaflet tension $\Sigma_{il} = -0.82\, k_{\text{B}}T/d^2$ whereas the outer leaflets are stretched by the positive leaflet tension $\Sigma_{ol} = +0.87\, k_{\text{B}}T/d^2$ (Lipowsky et al., 2023). Thus, both vesicle bilayers experience the initial stress asymmetry $\Delta\Sigma_{\text{ve}} = \Sigma_{ol} - \Sigma_{il} = 1.69\, k_{\text{B}}T/d^2$. After slightly deflating both vesicles from volume $\nu = 0.8$ to volume $\nu = 0.7$, the two vesicles start to adhere to each other, transform into two oblate shapes, and reach a stable adhesive state after about 20 μs without fusion (Lipowsky et al., 2023).

On the other hand, if we reshuffle only 100 lipids from the outer to the inner leaflet, thereby keeping the total lipid number in both leaflets at the constant value $N_{ol} + N_{il} = 10100$, we increase the outer leaflet tension to $\Sigma_{ol} = +1.02\, k_B T/d^2$ and decrease the inner leaflet tension to $\Sigma_{il} = -1.02\, k_B T/d^2$, which implies a moderate increase of the initial stress asymmetry from $\Delta\Sigma_{\mathrm{ve}} = 1.69\, k_B T/d^2$ to $\Delta\Sigma_{\mathrm{ve}} = 2.04\, k_B T/d^2$. As a consequence of this increased stress asymmetry, the two vesicles undergo a fast fusion process, which is completed within $0.3\,\mu$s, even without any intermediate reduction of the vesicle volumes (Lipowsky et al., 2023).

5.8 Membrane architecture of endoplasmic reticulum

Finally, let us briefly look at the fascinating architecture of the ER, a membrane-bound organelle that is found in all eukaryotic cells. In fact, each of these cells contains only one ER, which extends, however, throughout the whole cell by forming a continuous network of membrane nanotubes connected by three-way junctions, see the light microscopy image in Fig. 25a.

5.8.1 Multiscale architecture of ER membrane

The membrane architecture of the ER involves a hierarchy of length scales. The smallest supramolecular scale is provided by the thickness of the ER membrane which is of the order of 4 nm. Mitra et al. (2004) The ER membrane forms membrane nanotubes with a width that varies from about 50 nm to about 100 nm, depending on the organism and the cell type. The nanotubes are connected by three-way junctions, at which three nanotubes meet. The predominance of three-way junctions can be understood in terms of Steiner minimal trees (Lipowsky, 2022; Lipowsky et al., 2023a). The junctions form the vertices of irregular polygons, which are clearly visible in Fig. 25a. Even though the small ER section in Fig. 25a appears to be two-dimensional, the nanotubes and three-way junctions form a network that is truly three-dimensional, in analogy to Steiner minimal trees in three dimensions. The average mesh size of this nanotubular network is of the order of 1 μm. Finally, the nanotubular network extends across the whole eukaryotic cell, which has a typical extension of more than 50 μm.

5.8.2 Bicontinuous structure and topological genus

In spite of its complex architecture, the whole nanotubular network of the ER is formed by a single membrane which encloses a continuous nanofluidic network of water channels (Dayel et al., 1999; Holcman et al., 2018;

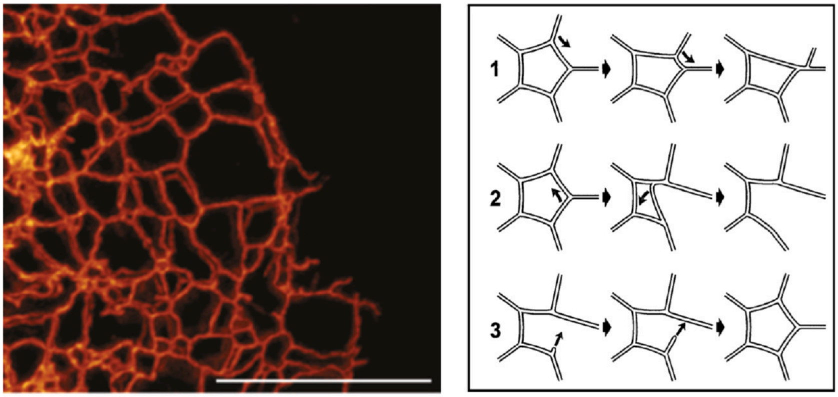

(a)

(b)

Fig. 25 (a) Nanotubular network of the peripheral endoplasmic reticulum (ER) with a very high topological genus, which is equal to the number of irregular polygons formed by the membrane nanotubes. Scale bar: 10 μm (Obara et al., 2023) Reprinted with permission of Jennifer Lippincott-Schwartz; and (b) Dynamic processes of sliding, ring closure, and branching as shown in row 1, 2, and 3, respectively. Ring closure removes one polygon from the network, thereby reducing the genus of the ER membrane by $\Delta\mathfrak{g} = -1$, whereas branching creates a new polygon which increases this genus by $\Delta\mathfrak{g} = +1$. *Reprinted with permission from Ref Baumann, O. & Walz, B. (2001). Endoplasmic reticulum of animal cells and its organization into structural and functional domains. International Review of Cytology, 205. [Copyright 2001, Elsevier].*

Obara et al., 2023). The continuity of the ER lumen has been demonstrated by monitoring the diffusion of fluorescently labeled molecules, using a variety of experimental techniques such as fluorescence recovery (Dayel et al., 1999) and single particle tracking (Holcman et al., 2018; Obara et al., 2023). As a consequence, the ER membrane creates a bicontinuous structure that partitions the intracellular space into two separate, interpenetrating subcompartments, provided by the lumen of the ER network and by the surrounding cytosol (Lipowsky et al., 2023a).

For a network of membrane nanotubes and junctions as formed by the ER membrane, the topological genus $\mathfrak{g}$ is equal to the number of polygons within this network. The optical image in Fig. 25a corresponds to a small section across the peripheral region of the ER, displaying more than 40 polygons which implies the topological genus $\mathfrak{g} > 40$ for this ER section. Fluorescence microscopy images of the whole organelle (Valm et al., 2017) indicate that the ER is built up from several thousands of polygons and, thus, has a very large topological genus.

5.8.3 Tensile forces and junction dynamics

Each three-way junction is subject to three tensile forces arising from the three nanotubes that meet at the junction. As long as the junction does not move, the three forces balance each other. This force balance explains the predominance of contact angles close to 120 degree between the nanotubes (Lipowsky et al., 2023a). Sometimes, the junctions are observed to move as shown in Fig. 25b. A moving junction implies that the tensile forces at this junction become temporarily unbalanced.

Three types of movements have been reported for three-way junctions in vivo. (Lee & Chen, 1988; Baumann & Walz, 2001). First, the sliding motion of one junction as displayed in the upper row of Fig. 25b moves the junction along one edge of a polygon, merges this moving junction into a transient four-way junction, which subsequently splits up into two new three-way junctions. This sliding process does not involve any fission or fusion of the membrane nanotubes and, thus, does not change the topological genus of the ER.

Second, during ring closure as shown in the middle row of Fig. 25b, one junction of a polygon merges successively with the other junctions of this polygon, which eventually leads to the elimination of one edge from the polygon. This process involves a single fission event of the ER membrane and locally decreases the genus of the ER by $\Delta\mathfrak{g} = -1$. Third, branching as in the lower row of Fig. 25b leads to a new tubule with a free end. Fusion of this free end with another tubule then creates a new junction and locally increases the genus of the ER by $\Delta\mathfrak{g} = +1$.

The three junction movements in Fig. 25b seem to affect only the local neighborhood of the junction under consideration. It is not known to what extent these movements are present in the whole nanotubular network of the ER. Likewise, the frequency with which these movements occur in a given subregion remains to be studied. If ring closure is more frequent than branching, the nanotubular network will decay by membrane fission. If branching is more frequent than ring closure, the network will grow by membrane fusion.

6. Summary and outlook

This review describes recent insights into the remodeling of biomembranes and vesicles. The remodeling processes considered here include the remodeling of vesicle shapes in Sections 2 and 3, stress-induced flip-flops and instabilities of lipid bilayers in Section 4, and topological transformations of vesicles in Section 5. These different processes are studied for two synthetic membrane systems as provided by giant vesicles and nanovesicles.

For giant vesicles, we start with the formation of two-sphere shapes, which may involve out-buds as in Fig. 1 or in-buds as in Fig. 2. The membrane necks that connect the two spherical membrane segment can be characterized by their effective mean curvature $M_{ij}^{\rm eff}$ as defined in Eq. (9). The sign of this curvature allows us to distinguish positive necks with $M_{ij}^{\rm eff} > 0$ from negative necks with $M_{ij}^{\rm eff} < 0$. This distinction also applies to multispheres consisting of more than two spheres connected by more than one membrane neck. In fact, all necks of a multisphere are either positive or negative, which allows us to distinguish positive from negative multispheres as in Fig. 8.

Two-sphere vesicles have also been observed for the complete engulfment of condensate droplets, see Fig. 7, and play a prominent role for phase-separated membranes with several intramembrane domains (Julicher & Lipowsky, 1996; Lipowsky, 2024) as well as for the endo- and exocytosis of nanoparticles (Agudo-Canalejo & Lipowsky, 2016). More details on multispheres can be found in Ref. Lipowsky (2022a), more details on the remodeling of membranes by condensate droplets in Ref. Lipowsky (2023).

Another recent development related to giant vesicles is the controlled remodeling of their shape by His-tagged proteins as described in Section 2.3. This development is based on the fine-tuning of the spontaneous curvature by low densities of membrane-bound proteins, which has been demonstrated for His-tagged GFP in a systematic and quantitative manner (Steinkühler et al., 2020). This controlled variation of the spontaneous curvature is also crucial for the fission of the closed membrane necks, which leads to the division of giant vesicles by increasing the GFP concentration in the exterior solution (Steinkühler et al., 2020).

The shape transformations of nanovesicles, as displayed in Figs. 10 and 11, resemble those of giant vesicles in Figs. 1 and 2, respectively. In fact, the volume represents an important shape parameter for both types of vesicles but the second shape parameter for nanovesicles is provided by the stress asymmetry between the two leaflet tensions of the lipid bilayers, as defined in Eq. (19), rather than by the spontaneous curvature as for giant vesicles. In order to obtain the leaflet tensions, one has to compute the average position of the molecular interface between the two leaflets. For this computation, two protocols have been particularly useful, the CHAIN protocol (Ghosh et al., 2019; Sreekumari & Lipowsky, 2022) and the VORON protocol (Zamaletdinov et al., 2023), both of which are described in Appendix B. The two leaflet tensions define a two-dimensional parameter space as in Fig. 14.

Large stress asymmetries lead to instabilities of lipid bilayers as described in Section 4. Two types of instabilities can be distinguished. First, large stress asymmetries lead to transbilayer flip-flops of lipids from one leaflet to the other. These flip-flops can be characterized by cumulative distribution functions as in Fig. 16. For nanovesicles, the distribution functions have a sigmoidal shape which implies that the vesicle bilayers undergo an ageing process. Second, in addition to flip-flops, large stress asymmetries also lead to structural instabilities of the lipid bilayers. One example for such an instability is shown in Fig. 17. More details on leaflet tensions and stress asymmetries can be found in Ref. Lipowsky et al. (2023).

Topological transformations of vesicles by membrane fission and fusion are addressed in Section 5. The simplest examples are provided by the fission of two-sphere vesicles and the fusion of two spherical vesicles. Each individual fission and fusion event involves the formation of a membrane neck as in Fig. 3. The free energy landscapes for fusion and fission are displayed in Fig. 18. For negative values of the Gaussian curvature modulus, membrane fission is an exergonic (downhill) process whereas membrane fusion is an endergonic (uphill) process.

The endocytosis of small condensate droplets by nanovesicles has been recently observed in molecular dynamics simulations (Ghosh et al., 2023) as described in Section 5.6. Two different endocytic pathways have been observed, which proceed via axisymmetric and non-axisymmetric shapes of the vesicle-droplet systems. The axisymmetric pathway involves a circular contact line between droplet and vesicle as well as an axisymmetric membrane neck that undergoes fission as in Fig. 22. The non-axisymmetric pathway leads to a tight-lipped shape of the closed membrane neck, which prevents the fission of this neck as in Fig. 23. The axisymmetric and non-axisymmetric pathways are observed for positive and negative line tensions of the contact line tension λ_{cl}, as follows from Fig. 24.

Interesting topics for future simulation studies include the influence of the stress asymmetries on the fission and fusion of nanovesicles. The simulation snapshots in Fig. 20 represent the results of preliminary simulations by Rikhia Ghosh (Lipowsky et al., 2023) and remain to be corroborated by more systematic studies. Likewise, recent simulations by

Aparna Sreekumari (Lipowsky et al., 2023) provide evidence for the formation of tight-lipped membrane necks during the engulfment of rigid nanoparticles. Because of their elongated shape, the latter necks do not undergo fission. On the other hand, for sufficiently large stress asymmetries, circular membrane necks should be formed, which do undergo fission and lead to particle endocytosis.

It would be highly desirable to develop experimental methods by which one can measure and modify the leaflet tensions of lipid bilayers and nanovesicles. Because the rate of lipid flip-flops depends on the stress asymmetry between the two leaflet tensions, see Fig. 16, additional insight into these tensions could be obtained from experiments that measure how the flip-flop rates vary when we expose the bilayers to different external conditions. One approach is provided by osmotic deflation and inflation of nanovesicles, see the VID data in Fig. 14.

Fusion and fission processes also generate the multiscale membrane architecture of the ER as briefly described in Section 5.8. Many aspects of this architecture are still poorly understood. A detailed analysis of the experimental literature has led to the proposal that the nanotubular network of the ER is subject to a significant membrane tension. (Lipowsky et al., 2023a) This proposal can be scrutinized by experiments on giant vesicles with reconstituted membrane proteins.

Several topics reviewed here are also addressed in other chapters of this book. Giant vesicles with asymmetric bilayer membranes are considered by T. Enoki et al. Biomolecular condensates on solid-supported bilayers are addressed by T. Baumgart et al. Numerical methods to solve the local shape equation of curvature elasticity are described by P. Rangamani et al. Improved error estimates for the computation of stress profiles are discussed by M. Deserno et al. Experimental techniques to study lipid flip-flops are addressed by D. Marquardt et al.

Acknowledgements

I thank all my coworkers for enjoyable and fruitful interactions. The recent experimental studies were performed in collaboration with Tripta Bhatia, Jan Steinkühler, Ziliang Zhao, Shreya Pramanik, Amelie S. Benk, Miroslaw Tarnawski, Joachim P. Spatz, and Rumiana Dimova. The recent theoretical and computational studies have been pursued together with Rikhia Ghosh, Vahid Satarifard, Aparna Sreekumari, Miftakh Zamaletdinov, Markus Miettinen, and Andrea Grafmüller. I also acknowledge the stimulating scientific environment of the Max Planck School Matter to Life, supported by the German Federal Ministry of Education and Research (BMBF) in collaboration with the Max Planck Society and the Max Planck Institute of Colloids and Interfaces.

Appendix A. Computation of bilayer tension

By definition, the local stress within a lipid bilayer is equal to the negative local pressure. Therefore, stress profiles are equivalent to pressure profiles. From an intuitive point of view, the local stress is positive close to the interface between a headgroup layer and the adjacent aqueous solution, because this interface can reduce its interfacial free energy by reducing its area, whereas the local stress is negative in the hydrophobic core, corresponding to a positive pressure arising from the confined hydrocarbon chains. It is interesting to note that the stress profiles as obtained by DPD simulations corroborate this intuitive picture (Rozycki & Lipowsky, 2015; Ghosh et al., 2019). Before stress profiles for planar bilayers were computed via molecular dynamics simulations, they have been described in a qualitative manner (Israelachvili et al., 1980; Helfrich, 1981; Cantor, 1997) and were studied by a statistical mechanical model for the hydrocarbon lipid chains (Szleifer et al., 1990) as well as by a local density functional (Gompper & Klein, 1992).

Values for the bilayer tension Σ were first reported from all-atom molecular dynamics simulations of DPPC bilayers (Feller et al., 1995). The latter study revealed, however, that the bilayer tension undergoes large fluctuations in such atomistic simulations, which make it difficult to obtain reliable tension values. The first stress profiles across planar lipid bilayers were reported in (Goetz & Lipowsky, 1998) where the underlying molecular model used a united-atom approach.

A.1 Anisotropic pressure tensor for planar bilayers

For a planar bilayer with periodic boundary conditions, the symmetry of the lipid-water system implies that the components of the local stress or pressure tensor, **P**, depend only on the Cartesian coordinate z perpendicular to the bilayer and has the general form (Goetz & Lipowsky, 1998)

$$\mathbf{P} = P_\mathrm{T}(z)[\mathbf{e_x} \otimes \mathbf{e_x} + \mathbf{e_y} \otimes \mathbf{e_y}] + P_\mathrm{N}\, \mathbf{e_z} \otimes \mathbf{e_z} \tag{A1}$$

with the tangential component $P_\mathrm{T}(z)$ and the normal component P_N where $\mathbf{e_x}$, $\mathbf{e_y}$, and $\mathbf{e_z}$ are orthogonal unit vectors and the symbol $\otimes$ represents the dyadic product. Furthermore, all components of the divergence of the pressure tensor, which is a vector with the Cartesian components $\sum_j \partial P_{ij}/\partial x_j$, must vanish (Schofield & Henderson, 1982; Rowlinson & Widom, 1989). In the present context, the latter requirement leads to $\partial P_{zz}/\partial z = 0$ which implies that $P_{zz} = P_\mathrm{N}$ does not depend on z and is constant throughout the simulation box. The tangential and normal components, $P_\mathrm{T}(z)$ and P_N, of the pressure tensor determine the z-dependent stress profile

$$s(z) \equiv P_\mathrm{N} - P_\mathrm{T}(z) \tag{A2}$$

across the bilayer. Note that positive stress $s > 0$ implies local stretching whereas negative stress $s < 0$ describes local compression. The bilayer tension Σ is then obtained from

$$\Sigma \equiv \int \mathrm{d}z\, s(z) = \int \mathrm{d}z\, [P_\mathrm{N} - P_\mathrm{T}(z)]. \tag{A3}$$

Because a planar liquid–liquid interface has the same symmetry as a planar bilayer, the pressure tensor of such an interface has the same general form as in Eq. (A1) and the interfacial tension and the stress profile can also be expressed in terms of the tangential and normal components of the pressure tensor as in Eqs. (A2) and (A3). For planar liquid–liquid interfaces, the pressure tensor and the interfacial tension have been theoretically studied for a long time (Bakker, 1928; Kirkwood & Buff, 1949; Irving & Kirkwood, 1950; Harasima, 1958; Schofield & Henderson, 1982; Rowlinson & Widom, 1989). These studies showed that the normal and tangential components of the pressure tensor can be divided up into a kinetic term and an interaction term.

The thermal average over the kinetic term is equal to $\rho(z)\delta_{ij}$ which is proportional to the local particle number density $\rho(z)$ but does not contribute to the stress profile $s(z) = P_{\mathrm{N}} - P_{\mathrm{T}}(z)$ in Eq. (A2) because it cancels out from this difference. The interaction terms of the pressure tensor components are more complex and depend on the interaction potentials between the particles. Furthermore, these interaction terms involve contours between interacting particles, which can be chosen in different ways (Irving & Kirkwood, 1950; Harasima, 1958). Using straight contours as in (Irving & Kirkwood, 1950), we generalized the theory for planar liquid–liquid interfaces as described in (Schofield & Henderson, 1982) to planar lipid bilayers (Goetz & Lipowsky, 1998). The resulting Goetz-Lipowsky protocol has been used to compute the stress profiles for all planar bilayers studied by our group (Rozycki & Lipowsky, 2015; Miettinen & Lipowsky, 2019; Sreekumari & Lipowsky, 2022; Lipowsky et al., 2023).

Because the pressure tensor is not unique (Irving & Kirkwood, 1950; Harasima, 1958; Schofield & Henderson, 1982; Rowlinson & Widom, 1989), the protocol for its calculation is not unique either. Another protocol is based on central force decomposition, which leads to a symmetric pressure tensor (Vanegas et al., 2014; Nakagawa & Noguchi, 2016). One disadvantage of the latter protocol is that it is ill-defined when three beads attain a collinear or four beads a coplanar configuration. In particular, central force decomposition cannot be used for the dihedral potentials which are present in the Martini force field for the glycolipid GM1 (Miettinen & Lipowsky, 2019).

A.2 Anisotropic pressure tensor for spherical nanovesicles

For a spherical nanovesicle, the components of the local stress or pressure tensor depend on the radial coordinate r. The pressure tensor then has the general form (Nakamura et al., 2015; Satarifard et al., 2018; Ghosh et al., 2019)

$$\mathbf{P} = P_{\mathrm{N}}(r)\,\mathbf{e}_r \otimes \mathbf{e}_r + P_{\mathrm{T}}(r)\left[\mathbf{e}_\theta \otimes \mathbf{e}_\theta + \mathbf{e}_\phi \otimes \mathbf{e}_\phi\right] \tag{A4}$$

with the normal component $P_{\mathrm{N}}(r)$ and the tangential component $P_{\mathrm{T}}(r)$ where $\mathbf{e}_r$, $\mathbf{e}_\theta$, and $\mathbf{e}_\phi$ are orthogonal unit vectors for the spherical coordinate system and the symbol $\otimes$ represents the dyadic product. The numerical values of $P_{\mathrm{N}}(r)$ and $P_{\mathrm{T}}(r)$ as well as the r-dependent stress profile

$$s(r) \equiv P_{\mathrm{N}}(r) - P_{\mathrm{T}}(r) \tag{A5}$$

can be calculated using the computational method described in (Nakamura et al., 2015; Satarifard et al., 2018; Ghosh et al., 2019). We found that the stress profile $s(r)$ changes strongly when we reshuffle lipids from one leaflet to the other, thereby changing the lipid numbers N_{ol} and N_{il} for constant $N_{ol} + N_{il}$. The bilayer tension Σ of the vesicle bilayer is taken to be

$$\Sigma \equiv \int_0^\infty \mathrm{d}r\,\left[P_{\mathrm{N}}(r) - P_{\mathrm{T}}(r)\right] = \int_0^\infty \mathrm{d}r\,s(r). \tag{A6}$$

in analogy to the bilayer tension of a planar bilayer as given by Eq. (A3) (Ghosh et al., 2019; Sreekumari & Lipowsky, 2022).

It is instructive to compare the mechanical bilayer tension Σ of a spherical vesicle as defined by Eq. (A6) with the interfacial tension Σ_{int} of a spherical liquid-liquid interface. The interfacial tension Σ_{int} can be defined in two ways: (i) Thermodynamically via an expansion of the system's free energy in powers of the system size; and (ii) Mechanically via the work expended to increase the area of the interface. In order to reconcile the mechanical and the thermodynamic route to interfacial tension, Gibbs dividing surfaces or "surfaces of tension" have been considered (Buff, 1956; Boruvka & Neumann, 1977; Rowlinson & Widom, 1989). As a consequence, one needs to solve two coupled equations to determine both the interfacial tension Σ_{int} and the position $r = R_{\text{int}}$ of the Gibbs dividing surface. In contrast, our computational studies of bilayer tension Σ were based on the mechanical definition of this tension as provided by Eqs. (A3) and (A6) which do not involve a Gibbs dividing surface. However, to decompose the bilayer tension into two leaflet tensions, we have to consider another surface, the midsurface of the lipid bilayer, the computation of which is described in the following Appendix B (Rozycki & Lipowsky, 2015; Ghosh et al., 2019; Miettinen & Lipowsky, 2019; Sreekumari & Lipowsky, 2022).

Appendix B. Computation of leaflet tensions

The molecular interface between the two leaflets of a bilayer undergoes thermally excited shape fluctuations as visualized in Fig. 12. The midsurface of such a lipid bilayer is defined by the average position of this molecular interface. For a spherical nanovesicle, this average position is described by the radial coordinate $r = r_{\text{mid}}$. The leaflet tensions Σ_{il} and Σ_{ol} of the inner and outer leaflet are then computed by (Ghosh et al., 2019; Sreekumari & Lipowsky, 2022)

$$\Sigma_{il} = \int_0^{r_{\text{mid}}} \mathrm{d}r\; s(r) \quad \text{and} \quad \Sigma_{ol} = \int_{r_{\text{mid}}}^{r_{\text{max}}} \mathrm{d}r\; s(r), \tag{B1}$$

which represents the decomposition of the bilayer tension Σ in Eq. (A6) according to $\Sigma = \Sigma_{il} + \Sigma_{ol}$. The radius r_{max} is an appropriate upper cut-off for the integration. In practice, one can reduce the integration over r to a small interval around the vesicle bilayer because the stress profile $s = s(r)$ decays rapidly to zero as we move away from this bilayer.

B.1 CHAIN protocol for computation of r_{mid}

The simplest procedure to determine the midsurface radius $r = r_{\text{mid}}$ is provided by the CHAIN protocol, which uses the local extremum of the hydrophobic chain density to obtain r_{mid}. The leaflet tension data in Fig. 11 have been obtained via this protocol. The data in Fig. 13a are obtained for vesicle volume $\nu = 1$, using $N_{\text{W}}^{\text{isp}} = 90\,400$ for the initial number of interior water beads. The data in Fig. 13b are computed for tensionless vesicle bilayers after slightly deflating the vesicles to $\nu = \nu_0 < 1$. For the five values of N_{ol} displayed in Fig. 13b, the nanovesicles attain OLT states with vanishing bilayer tension, $\Sigma = \Sigma_{il} + \Sigma_{ol} = 0$, for rescaled volumes ν_0 within the range $0.966 \le \nu_0 \le 0.978$. (Ghosh et al., 2019) All OLT states of the nanovesicles are obtained from the reference state with tensionless leaflets by reshuffling lipids from one leaflet to the other and adjusting the rescaled volume ν of the vesicle to $\nu = \nu_0$.

B.2 VORON protocol for computation of r_{mid}

The VORON protocol is based on Voronoi tesselation of all molecules or beads within the simulation box. (Zamaletdinov et al., 2023) Voronoi tessellation assigns a polyhedral Voronoi cell to each bead of the molecular model. The volumes of the inner and outer leaflets of the vesicle bilayer, V_{il} and V_{ol}, are computed by summing up all bead volumes located within each leaflet. The volumes per lipid of the inner and outer leaflets are then obtained by dividing the leaflet volumes V_{il} and V_{ol} by the number of lipids, N_{il} and N_{ol}, assembled in these leaflets.

To compute the radial coordinate $r = r_{\text{mid}}$ for the midsurface position of the vesicle bilayer, we consider a cubic simulation box with volume L^3, which is divided up into two separate water compartments by the closed surface of the vesicle, the inner water compartment with volume $V_{i\text{W}}$ and the outer water compartment with volume $V_{o\text{W}}$. The midsurface radius $r = r_{\text{mid}}$ of the vesicle bilayer can then be computed using two geometric relationships. The first geometric relationship has the form

$$\frac{4\pi}{3} r_{\text{mid}}^3 = V_{il} + V_{i\text{W}}, \tag{B2}$$

and relates the midsurface radius r_{mid} to the volume V_{il} of the inner leaflet and the volume $V_{i\text{W}}$ of the inner water compartment. The second geometric relationship is given by

$$\frac{4\pi}{3} r_{\text{mid}}^3 = L^3 - V_{o\text{W}} - V_{ol}, \tag{B3}$$

which depends on the volume L^3 of the simulation box, the volume $V_{o\text{W}}$ of the outer water compartment, and the volume V_{ol} of the outer leaflet. The two relationships in Eqs. (B2) and B3 give identical values for r_{mid} within the numerical accuracy (Zamaletdinov et al., 2023).

References

Agudo-Canalejo, J., & Lipowsky, R. (2016). Stabilization of membrane necks by adhesive particles, substrate surfaces, and constriction forces. *Soft Matter, 12*, 8155–8166.

Alberts, B., Bray, D., Johnson, A., Lewis, J., Raff, M., Roberts, K., & Walter, P. (1998). *Essential cell biology: An introduction to the molecular biology of the cell*. New York: Garland.

Albertsson, P. A. (1986). *Partition of Cell Particles and Macromolecules: Separation and purification of biomolecules cell organelles membranes, and cells in aqueous polymer two-phase systems and their use in biochemical analysis and biotechnology* (3rd ed.), Wiley.

Andes-Koback, M., & Keating, C. D. (2011). Complete budding and asymmetric division of primitive model cells to produce daughter vesicles with different interior and membrane compositions. *JACS, 133*(24), 9545–9555.

Arpino, J. A. J., Rizkallah, P. J., & Jones, D. D. (2012). Crystal structure of enhanced green fluorescent protein to 1.35 a resolution reveals alternative conformations for Glu222. *PLOS One,* 7(10), e47132.

Bakker, G. (1928). *Kapillarität und Oberflächenspannung, Vol. 6 of Handbuch der Experimentalphysik*. Leipzig: Akademische Verlagsgesellschaft.

Banani, S. F., Lee, H. O., Hyman, A. A., & Rosen, M. K. (2017). Biomolecular condensates: Organizers of cellular biochemistry. *Nature Reviews Molecular Cell Biology, 18*, 285–295.

Bartelt, S. M., Chervyachkova, E., Steinkuehler, J., Ricken, J., Wieneke, R., Tampé, R., … Wegner, S. V. (2018). Dynamic blue light-switchable protein patterns on giant unilamellar vesicles. *Chemical Communications, 54*, 948–951.

Bassereau, P., & Sens, P. (2018). *Physics of biological membranes*. Cham, Switzerland: Springer Nature Switzerland AG.

Baumann, O., & Walz, B. (2001). Endoplasmic reticulum of animal cells and its organization into structural and functional domains. *International Review of Cytology, 205*.

Baxa, U. (2018). Imaging of liposomes by transmission electron microscopy. *1682*. Springer Science+Business Media.

Berndl, K., Käs, J., Lipowsky, R., Sackmann, E., & Seifert, U. (1990). Shape transformations of giant vesicles: Extreme sensitivity to bilayer asymmetry. *Europhysics Letters, 13*, 659–664.

Berry, J., Weber, S. C., Vaidya, N., Haatajaa, M., & Brangwynne, C. P. (2015). RNA transcription modulates phase transition-driven nuclear body assembly. *Proceedings of the National Academy of Sciences USA, 112*, E5237–E5245.

Bhatia, T., Christ, S., Steinkühler, J., Dimova, R., & Lipowsky, R. (2020). Simple sugars shape giant vesicles into multispheres with many membrane necks. *Soft Matter, 16*, 1246–1258.

Bonifacino, J. S., & Glick, B. S. (2004). The mechanisms of vesicle budding and fusion. *Cell, 116*, 153–166.

Boruvka, L., & Neumann, A. W. (1977). Generalization of the classical theory of capillarity. *The Journal of Chemical Physics. 66*, 5464–5476.

Brangwynne, C. P., Eckmann, C. R., Courson, D. S., Rybarska, A., Hoege, C., Gharakhani, J., … Hyman, A. A. (2009). Germline P granules are liquid droplets that localize by controlled dissolution/condensation. *Science, 324*, 1729–1732.

Buff, F. P. (1956). Curved fluid interfaces. I. The generalized gibbs-kelvin equation. *The Journal of Chemical Physics. 25*, 146–153.

Bungenberg de Jong, H. G., & Kruyt, H. R. (1929). Coacervation (Partial miscibility in colloid systems)(Preliminary Communication). *Proceedings of the Koninklijke Nederlandse Akademie van Wetenschappen, 32*, 849–856.

Cantor, R. S. (1997). Lateral pressures in cell membranes: A mechanism for modulation of protein function. *The Journal of Physical Chemistry. B, 101*, 1723–1725.

Cox, D. R. (1962). *Renewal theory*. Methuen and Co Ltd.

Crowe, C. D., & Keating, C. D. (2018). Liquid–liquid phase separation in artificial cells. *Interface Focus, 8*, 20180032.

Dayel, M. J., Hom, E. F. Y., & Verkman, A. S. (1999). Diffusion of green fluorescent protein in the aqueous-phase lumen of endoplasmic reticulum. *Biophysical Journal. 76*, 2843–2851.

de Gennes, P.-G., & Taupin, C. (1982). Microemulsions and the flexibility of oil/water interfaces. *The Journal of Physical Chemistry. 86*, 2294–2304.

Derzhanski, A., Petrov, A. G., & Mitov, M. D. (1978). Molecular asymmetry and saddle-splay elasticity in lipid bilayers. *Annales de Physique, 3*, 297.

Deserno, M. (2018). Gaussian curvature, membrane topology, and the energetics of membrane fusion. *Journal of Physics D: Applied Physics. 51*, 343001.

Deuling, H. J., & Helfrich, W. (1976). The curvature elasticity of fluid membranes: A catalogue of vesicle shapes. *Journal de Physique, 37*, 1335–1345.

Dimova, R., & Lipowsky, R. (2017). Giant vesicles exposed to aqueous two-phase systems: Membrane wetting, budding processes, and spontaneous tubulation. *Advanced Materials Interfaces, 4*, 1600451.

Dimova, R., & Marques, C. (2019). *The giant vesicle book*. Taylor & Francis.

do Carmo, M. P. (1976). *Differential geometry of curves and surfaces*. Englewood Cliffs, NJ: Prentice-Hall.

Döbereiner, H.-G., Evans, E., Kraus, M., Seifert, U., & Wortis, M. (1997). Mapping vesicle shapes into the phase diagram: A comparison of experiment and theory. *Physical Review E, 55*(4), 4458–4474.

Dragicevic-Curic, N., Scheglmann, D., Albrecht, V., & Fahr, A. (2008). Temoporfin-loaded invasomes: Development, characterization and in vitro skin penetration studies. *Journal of Controlled Release, 127*, 59–69.

Esquena, J. (2016). Water-in-water (W/W) emulsions. *Current Opinion in Colloid & Interface Science, 25*, 109–119.

Feller, S. E., Zhang, Y., & Pastor, R. W. (1995). Computer simulation of liquid/liquid intrefaces. II. Surface tension–area dependence of a bilayer and monolayer. *The Journal of Chemical Physics, 103*, 10267–10276.

Foley, S., & Deserno, M. (2020). Stabilizing leaflet asymmetry under differential stress in a highly coarse-grained lipid membrane model. *Journal of Chemical Theory and Computation. 16*, 7195–7206.

Fritsch, A. W., Diaz-Delgadillob, A. F., Adame-Arana, O., Hoege, C., Mittasch, M., Kreysing, M., ... Weber, C. A. (2021). Local thermodynamics govern formation and dissolution of *Caenorhabditis elegans* P granule condensates. *PNAS, 118*(37), e2102772118.

Georgiev, V. N., Grafmüller, A., Bléger, D., Hecht, S., Kunstmann, S., Barbirz, S., Lipowsky, R., & Dimova, R. (2018). Area increase and budding in giant vesicles triggered by light: Behind the scene. *Advanced Science, 5*, 1800432.

Ghosh, R., Satarifard, V., & Lipowsky, R. (2023). Different pathways for engulfment and endocytosis of droplets by nanovesicles. *Nature Communications, 14*, 615.

Ghosh, R., Satarifard, V., Grafmüller, A., & Lipowsky, R. (2019). Spherical nanovesicles transform into a multitude of nonspherical shapes. *Nano Letters, 19*, 7703–7711.

Ghosh, R., Satarifard, V., Grafmüller, A., & Lipowsky, R. (2021). Budding and Fission of Nanovesicles induced by membrane adsorption of small solutes. *ACS Nano, 15*, 7237–7248.

Gibbs, J. W. (1906). *The Scientific papers of J. Willard Gibbs*. Longman, Green, and Co.

Goetz, R., & Lipowsky, R. (1998). Computer simulations of bilayer membranes: Self-assembly and interfacial tension. *The Journal of Chemical Physics. 108*, 7397–7409.

Gompper, G., & Klein, S. (1992). Ginzburg-Landau theory of aqueous surfactant solutions. *Journal de Physique II France, 2*, 1725–1744.

Gompper, G., & Kroll, D. M. (1995). Phase diagram and scaling behavior of fluid vesicles. *Physical Review E, 51*, 514–525.

Guo, L., & Shorter, J. (2015). It's raining liquids: RNA tunes viscoelasticity and Dynamics of membraneless organelles. *Molecular Cell, 60*, 189–192.

Han, T. W., Kato, M., Xie, S., Wu, L. C., Mirzaei, H., Pei, J., ... McKnight, S. L. (2012). Cell-free formation of RNA Granules: Bound RNAs Identify features and components of cellular assemblies. *Cell, 149*, 768–779.

Harasima, A. (1958). Molecular theory of surface tension. In I. Prigogine, & P. Debye (Vol. Eds.), *Advances in chemical physics. vol. 1. Advances in chemical physics* (pp. 203–237). Wiley volume 1.

Helfrich, W. (1973). Elastic properties of lipid bilayers: Theory and possible experiments. *Zeitschrift für Naturforschung, 28c*, 693–703.

Helfrich, W. (1981). Amphiphilic mesophases made of defects. In R. Balian, (Ed.). *Physics of defects* (pp. 715–755). Amsterdam: North-Holland Publishing Company.

Hildebrandt, S., & Tromba, A. (1985). *Mathematics and Optimal Form*. New York: American Scientific Library.

Holcman, D., Parutto, P., Chambers, J. E., Fantham, M., Young, L. J., Marciniak, S. J., ... Avezov, E. (2018). Single particle trajectories reveal active endoplasmic reticulum luminal flow. *Nature Cell Biology. 20*, 1118–1125.

Hossein, A., & Deserno, M. (2020). Spontaneous curvature, differential stress, and bending modulus of asymmetric lipid membranes. *Biophysical Journal, 118*, 624–642.

Hu, M., Briguglio, J. J., & Deserno, M. (2012). Determining the gaussian curvature modulus of lipid membranes in simulations. *Biophysical Journal. 102*(6), 1403–1410.

Irving, J. H., & Kirkwood, J. G. (1950). The statistical mechanical theory of transport processes. *The Journal of Chemical Physics. 18*, 817–829.

Israelachvili, J. N., Marcelja, S., & Horn, R. G. (1980). Physical principles of membrane organization. *Quarterly Reviews of Biophysics. 13*, 121–200.

Jain, S., Wheeler, J. R., Walters, R. W., Agrawal, A., Barsic, A., & Parker, R. (2016). ATPase-modulated stress granules contain a diverse proteome and substructure. *Cell, 164*, 487–498.

Jülicher, F., & Lipowsky, R. (1996). Shape transformations of inhomogeneous vesicles with intramembrane domains. *Physical Review E, 53*, 2670–2683.

Kirkwood, J. G., & Buff, F. P. (1949). The statistical mechanical theory of surface tension. *The Journal of Chemical Physics. 17*(3), 338–343.

Kozlov, M. M., Leikin, S. L., & Markin, V. S. (1989). Elastic properties of interfaces. *Journal of the Chemical Society, Faraday Transactions, 2*(85), 277–292.

Kusumaatmaja, H., Li, Y., Dimova, R., & Lipowsky, R. (2009). Intrinsic contact angle of aqueous phases at membranes and vesicles. *Physical Review Letters, 103*, 238103.

Lai, C.-D. (2014). *Generalized Weibull distributions*. Springer Briefs in Statistics. Springer.

Landau, L. D., & Lifshitz, E. M. (1986). *Theory of elasticity*. New York: Pergamon Press.

Lee, C., & Chen, L. B. (1988). Dynamic behavior of endoplasmic reticulum in living cells. *Cell, 54*, 37–46.

Li, P., Banjade, S., Cheng, H.-C., Kim, S., Chen, B., Guo, L., ... Rosen, M. K. (2012a). Phase transitions in the assembly of multivalent signalling proteins. *Nature, 483*, 336–341.

Li, Y., Kusumaatmaja, H., Lipowsky, R., & Dimova, R. (2012b). Wetting-induced budding of vesicles in contact with several aqueous phases. *The Journal of Physical Chemistry B, 116*, 1819–1823.

Li, X., Liu, Y., Wang, L., Deng, M., & Liang, H. (2009). Fusion and fission pathways of vesicles from amphiphilic triblock copolymers: A dissipative particle dynamics simulation study. *Physical Chemistry Chemical Physics. 11*, 4051–4059.

Li, L., Srivastava, S., Andreev, M., Marciel, A. B., de Pablo, J. J., & Tirrell, M. V. (2018). Phase behavior and salt partitioning in polyelectrolyte complex coacervates. *Macromolecules, 51*, 2988–2995.

Lin, Y., Protter, D. S. W., Rosen, M. K., & Parker, R. (2015). Formation and maturation of phase-separated liquid droplets by RNA-binding proteins. *Molecular Cell, 60*, 208–219.

Lipowsky, R. (2014). Coupling of bending and stretching deformations in vesicle membranes. *Advances in Colloid and Interface Science, 208*, 14–24.

Lipowsky, R. (2018). Response of membranes and vesicles to capillary forces arising from aqueous two-phase systems and water-in-water emulsions. *The Journal of Physical Chemistry. B, 122*, 3572–3586.

Lipowsky, R. (2018a). Curvature elasticity and multi-sphere morphologies. *Journal of Physics D: Applied Physics. 51*, 343001.

Lipowsky, R. (2018b). Understanding membranes and vesicles: A personal recollection of the last two decades. In P. Bassereau, & P. Sens (Eds.). *Physics of biological membranes* (pp. 1–44). Springer.

Lipowsky, R. (2019). Understanding giant vesicles: A theoretical perspective. In R. Dimova, & C. Marques (Eds.). *The giant vesicle book, chapter 5* (pp. 73–168). Taylor & Francis chapter 5.

Lipowsky, R. (2022). Remodeling of membrane shape and topology by curvature elasticity and membrane tension. *Adv. Biology, 6*, 2101020.

Lipowsky, R. (2022a). Multispherical shapes of vesicles highlight the curvature elasticity of biomembranes. *Advances in Colloid and Interface Science, 301*, 102613.

Lipowsky, R. (2023). Remodeling of biomembranes and vesicles by adhesion of condensate droplets. *Membranes, 13*, 223.

Lipowsky, R. (2024). Multispherical shapes of vesicles with intramembrane domains. *EPJE, 47*, 4.

Lipowsky, R., & Dimova, R. (2021). Introduction to remodeling of biomembranes. *Soft Matter, 17*, 214–221.

Lipowsky, R., Ghosh, R., Satarifard, V., Sreekumari, A., Zamaletdinov, M., Różycki, B., ... Grafmüller, A. (2023). Leaflet tensions control the spatio-temporal remodeling of lipid bilayers and nanovesicles. *Biomolecules, 13*, 926.

Lipowsky, R., Pramanik, S., Benk, A. S., Tarnawski, M., Spatz, J. P., & Dimova, R. (2023a). Elucidating the morphology of the endoplasmic reticulum: Puzzles and perspectives. *ACS Nano, 17*, 11957–11968.

Lipowsky, R., & Sackmann, E. (1995). *Structure and dynamics of membranes. volume 1 of Handbook of biological physics*. Amsterdam: Elsevier.

Lorenzen, S., Servuss, R.-M., & Helfrich, W. (1986). Elastic torques about membrane edges: A study of pierced egg lecithin vesicles. *Biophysical Journal. 50*, 565–572.

Miettinen, M., & Lipowsky, R. (2019). Bilayer membranes with frequent flip flops have tensionless leaflets. *Nano Letters. 19*, 5011–5016.

Mitra, K., Ubarretxena-Belandia, I., Taguchi, T., Warren, G., & Engelman, D. M. (2004). Modulation of the bilayer thickness of exocytic pathway membranes by membrane proteins rather than cholesterol. *Proceedings of the National Academy of Sciences. USA, 101*, 4083–4088.

Molliex, A., Temirov, J., Lee, J., Kim, H. J., Mittag, T., & Taylor, J. P. (2015). Phase separation by low complexity domains promotes stress granule assembly and drives pathological fibrillization. *Cell, 163*, 123–133.

Mui, B. L.-S., Döbereiner, H.-G., Madden, T. D., & Cullis, P. R. (1995). Influence of transbilayer area asymmetry on the morphology of large unilamellar vesicles. *Biophysical Journal, 69*, 930–941.

Nakagawa, K. M., & Noguchi, H. (2016). Nonuniqueness of local stress of three-body potentials in molecular simulations. *Physical Review E, 94*, 053304.

Nakamura, T., Kawamoto, S., & Shinoda, W. (2015). Precise calculation of the local pressure tensor in cartesian and spherical coordinates in LAMMPS. *Computer Physics Communications, 190*, 120–128.

Noguchi, H., & Takasu, M. (2002). Adhesion of nanoparticles to vesicles: A Brownian dynamics simulation. *Biophysical Journal. 83*, 299–308.

Obara, C. J., Moore, A. S., & Lippincott-Schwartz, J. (2023). Structural diversity within the endoplasmic reticulum—from the microscale to the nanoscale. *Cold Spring Harbor Perspectives in Biology, 15*, a041259.

Osserman, R. (1978). The Isoperimetric Inequality. *Bulletin of the American Mathematical Society, 84*, 1182–1238.

Pannuzzo, M., McDargh, Z. A., & Deserno, M. (2018). The role of scaffold reshaping and disassembly in dynamin driven membrane fission. *eLife, 7*, e39441.

Patel, A., Lee, H. O., Jawerth, L., Maharana, S., Jahnel, M., Hein, M. Y., ... Alberti, S. (2015). A liquid-to-solid phase transition of the ALS Protein FUS accelerated by disease mutation. *Cell, 162*, 1066–1077.

Pramanik, S., Steinkühler, J., Dimova, R., Spatz, J. P., & Lipowsky, R. (2022). Binding of his-tagged fluorophores to lipid bilayers of giant vesicles. *Soft Matter, 18*, 6372–6383.

Rinne, H. (2008). *The weibull distribution—a handbook*. Taylor & Francis.

Roux, A., Koster, G., Lenz, M., Sorre, B., Manneville, J.-B., Nassoy, P., & Bassereau, P. (2010). Membrane curvature controls dynamin polymerization. *PNAS, 107*(9), 4242–4246.

Rowlinson, J. S., & Widom, B. (1989). *Molecular theory of capillarity*. Oxford: Oxford University Press.

Różycki, B., & Lipowsky, R. (2015). Spontaneous curvature of bilayer membranes from molecular simulations: Asymmetric lipid densities and asymmetric adsorption. *The Journal of Chemical Physics, 142*, 054101.

Satarifard, V., Grafmüller, A., & Lipowsky, R. (2018). Nanodroplets at membranes create tight-lipped membrane necks via negative line tension. *ACS Nano, 12*, 12424–12435.

Schoeneberg, J., Pavlin, M. R., Yan, S., Righini, M., Lee, I.-H., Carlson, L.-A., ... Hurley, J. H. (2018). ATP-dependent force generation and membrane scission by ESCRT-III and Vps4. *Science, 362*, 1423–1428.

Schofield, P., & Henderson, J. R. (1982). Statistical mechanics of inhomogeneous fluids. *Proceedings of the Royal Society of London. Series A*, *379,* 231–246, 1982.

Seifert, U., Berndl, K., & Lipowsky, R. (1991). Shape transformations of vesicles: Phase diagram for spontaneous curvature and bilayer coupling model. *Physical Review A Letters, 44*, 1182–1202.

Seifert, U., Miao, L., Döbereiner, H.-G., & Wortis, M. (1992). Budding transition for bilayer fluid vesicles. In R. Lipowsky, D. Richter, & K. Kremer (Eds.). *The structure and conformation of amphiphilic membranes, Springer proceedings in physic* (pp. 93–96). Springer-Verlag.

Shillcock, J. C., & Lipowsky, R. (2002). Equilibrium structure and lateral stress distribution of amphiphilic bilayers from dissipative particle dynamics simulations. *The Journal of Chemical Physics. 117*, 5048–5061.

Shillcock, J., & Lipowsky, R. (2005). Tension-induced fusion of bilayer membranes and vesicles. *Nature Materials, 4*, 225–228.

Sing, C. E. (2017). Development of the modern theory of polymeric complex coacervation. *Advances in Colloid and Interface Science, 239*, 2–16.

Sreekumari, A., & Lipowsky, R. (2018). Lipids with bulky head groups generate large membrane curvatures by small compositional asymmetries. *The Journal of Chemical Physics. 149*, 084901.

Sreekumari, A., & Lipowsky, R. (2022). Large stress asymmetries of lipid bilayers and nanovesicles generate lipid flip-flops and bilayer instabilities. *Soft Matter, 18*, 6066–6078.

Steinkühler, J., Knorr, R. L., Zhao, Z., Bhatia, T., Bartelt, S., Wegner, S., ... Lipowsky, R. (2020). Controlled division of cell-sized vesicles by low densities of membrane-bound proteins. *Nature Communications, 11*, 905.

Svetina, S., & Žekš, B. (2002). Shape behavior of lipid vesicles as the basis of some cellular processes. *The Anatomical Record, 268*, 215–225.

Szleifer, I., Kramer, D., Ben-Shaul, A., Gelbart, W. M., & Safran, S. A. (1990). Molecular theory of curvature elasticity in surfactant films. *The Journal of Chemical Physics. 92,* 6800–6817.

Taylor, H. M., & Karlin, S. (1998). *An introduction to stochastic modelling* (3rd ed.,). San Diego: Academic Press.

Templer, R. H. (1995). On the area neutral surface of inverse bicontinuous cubic phases of lyotropic liquid crystals. *Langmuir, 11*, 334–340.

Urakami, N., Jimbo, T., Sakuma, Y., & Imai, M. (2018). Molecular mechanism of vesicle division induced by coupling between lipid geometry and membrane curvatures. *Soft Matter, 14*, 3018–3027.

Valm, A. M., Cohen, S., Legant, W. R., Melunis, J., Hershberg, U., Wait, E., ... Lippincott-Schwartz, J. (2017). Applying systems-level spectral imaging and analysis to reveal the organelle interactome. *Nature, 546*, 162–167.

Vanegas, J. M., Torres-Sánchez, A., & Arroyo, M. (2014). Importance of force decomposition for local stress calculations in biomembrane molecular simulations. *Journal of Chemical Theory and Computation. 10*, 691–702.

Varma, M., & Deserno, M. (2022). Distribution of cholesterol in asymmetric membranes driven by composition and differential stress. *Biophysical Journal, 121*, 4001–4018.

Weibull, W. (1951). A statistical distribution function of wide applicability. *Journal of Applied Mechanics, 18*, 293–297.

Winterhalter, M., & Helfrich, W. (1992). Bending elasticity of electrically charged bilayers: Coupled monolayers, neutral surfaces, and balancing stresses. *The Journal of Physical Chemistry. 96*, 327–330.

Xiao, J., & Goley, E. D. (2016). Redefining the roles of the FtsZ-ring in bacterial cytokinesis. *Current Opinion in Microbiology. 34*, 90–96.

Zamaletdinov, M., Miettinen, M., & Lipowsky, R. (2023). Probing the elastic response of lipid bilayers and nanovesicles to leaflet tensions via volume per lipid. *Soft Matter, 19*, 6929–6944.